HAL
open science

Extensional faulting on Tinos island, Aegean sea, Greece: How many detachments?

P. Brichau, U. Ring, A. Carter, Patrick Monie, R. Bolhar, D. Stockli, Maurice Brunel

To cite this version:

P. Brichau, U. Ring, A. Carter, Patrick Monie, R. Bolhar, et al.. Extensional faulting on Tinos island, Aegean sea, Greece: How many detachments?. Tectonics, 2007, 26 (4), pp.TC4009. 10.1029/2006TC001969 . hal-00407638

HAL Id: hal-00407638

https://hal.science/hal-00407638v1

Submitted on 26 Mar 2021

HAL is a multi-disciplinary open access archive for the deposit and dissemination of scientific research documents, whether they are published or not. The documents may come from teaching and research institutions in France or abroad, or from public or private research centers.

L'archive ouverte pluridisciplinaire **HAL**, est destinée au dépôt et à la diffusion de documents scientifiques de niveau recherche, publiés ou non, émanant des établissements d'enseignement et de recherche français ou étrangers, des laboratoires publics ou privés.

Extensional faulting on Tinos Island, Aegean Sea, Greece: How many detachments?

Stéphanie Brichau,[1] Uwe Ring,[2] Andrew Carter,[1] Patrick Monié,[3] Robert Bolhar,[2] Daniel Stockli,[4] and Maurice Brunel[3]

Received 16 March 2006; revised 16 January 2007; accepted 30 March 2007; published 26 July 2007.

[1] Zircon and apatite fission track (ZFT and AFT) and (U-Th)/He, $^{40}Ar/^{39}Ar$ hornblende, and U-Pb zircon ages from the granites of Tinos Island in the Aegean Sea, Greece, suggest, together with published ZFT data, that there are three extensional detachments on Tinos. The Tinos granites crosscut the Tinos detachment. Cooling of the granites was controlled by the Livadi detachment, which occurs structurally above the Tinos detachment. Our U-Pb zircon age is 14.6 ± 0.2 Ma and two $^{40}Ar/^{39}Ar$ hornblende ages are 14.4 ± 0.4 and 13.7 ± 0.4 Ma. ZFT and AFT ages go from 14.4 ± 1.2 to 12.2 ± 1.0 Ma and 12.8 ± 2.4 to 11.9 ± 2.0 Ma. (U-Th)/He ages are from 10.4 ± 0.2 to 9.9 ± 0.2 Ma (zircon) and 11.9 ± 0.5 to 10.0 ± 0.3 Ma (apatite). All ages decrease northeastward in the direction of hanging wall transport on the Livadi detachment and age-distance relationships yield a slip rate of 2.6 (+3.3 / −1.0) km Ma^{-1}. This rate is smaller than a published slip rate of 6.5 km Ma^{-1} for the Vari detachment, which is another detachment structurally above the Tinos detachment. Because of the different rates and because published ZFT ages from the footwall of the Vari detachment are ~10 Ma, we propose that the Vari detachment has to be distinguished from the older Livadi detachment. We discuss various models of how the extensional detachments may have evolved and prefer a scenario in which the Vari detachment cut down into the footwall of the Livadi detachment successively exhuming deeper structural units. The thermochronologic ages demonstrate the importance of quantitative data for constraining localization processes during extensional deformation. **Citation:** Brichau, S., U. Ring, A. Carter, P. Monié, R. Bolhar, D. Stockli, and M. Brunel (2007), Extensional faulting on Tinos Island, Aegean Sea, Greece: How many detachments?, *Tectonics*, *26*, TC4009, doi:10.1029/2006TC001969.

[1]School of Earth Sciences, University and Birkbeck College, London, UK.
[2]Department of Geological Sciences, University of Canterbury, Christchurch, New Zealand.
[3]Laboratoire Dynamique de la lithosphère, UMR-CNRS 5573, Université Montpellier II, Montpellier, France.
[4]Department of Geology, University of Kansas, Lawrence, Kansas, USA.

Copyright 2007 by the American Geophysical Union.
0278-7407/07/2006TC001969

1. Introduction

[2] The Hellenic subduction zone in the eastern Mediterranean is a world class example of a retreating subduction zone. Currently, extensional faulting occurs mainly in front of the magmatic arc but in the past it occurred both in front of, within and behind the arc. Most extensional detachments dip at similar low angles as the current subduction thrust and in part seem to have reactivated the latter as it moved outboard [*Lister et al.*, 1984; *Ring et al.*, 2001]. The majority of the Miocene detachments in the Cyclades operated in an intra-arc setting (Figure 1). Asthenospheric inflow into the intra-arc mantle wedge caused melting, granite intrusions and crustal weakening and these processes played in part an important role in the development of some of the Miocene detachments.

[3] The granites intruded into the footwalls of the Miocene detachments and a characteristic feature of these footwalls is that they cool rapidly as they are dragged toward the surface. Therefore low-temperature thermochronology is a powerful tool for establishing cooling and slip rates and the timing of the detachments. Zircon and apatite fission track (ZFT and AFT) and (U-Th)/He (ZHe and AHe) data, as well as $^{40}Ar/^{39}Ar$ mica ages have been used to constrain the timing, speed and footwall cooling rates of major Aegean extensional detachments. For the Messaria, Naxos/Paros, Mykonos, Vari and Simav detachments (Figure 1) reported time-averaged slip rates are >5–8 km Ma^{-1} [*John and Howard*, 1995; *Ring et al.*, 2003a, 2003b; *Kumerics et al.*, 2005; *Brichau et al.*, 2006, 2007; *Thomson and Ring*, 2006]. These five detachments are associated with huge syntectonic granites that intruded into their footwalls. The only so far known extensional fault that slipped at a distinctly smaller rate is the Pliocene/Recent Kuzey detachment in western Turkey (Figure 1) with a rate of ~2 km Ma^{-1} [*Gessner et al.*, 2001].

[4] In this study, we report U-Pb zircon, $^{40}Ar/^{39}Ar$ hornblende, ZFT, AFT, ZHe and AHe ages from the Tinos granites. All ages consistently decrease northeastward in the direction of hanging wall transport on the Livadi detachment. Age/distance relationships of our data suggest that the Livadi detachment slipped at a time-averaged rate of 2.6 (+3.3/−1.0) km Ma^{-1}, which is a slower rate than that of other syngranitic extensional detachments in the Aegean Sea.

2. Setting

[5] Previous studies showed that the Hellenides are made up by tectonic zones that are distinguished by rock type,

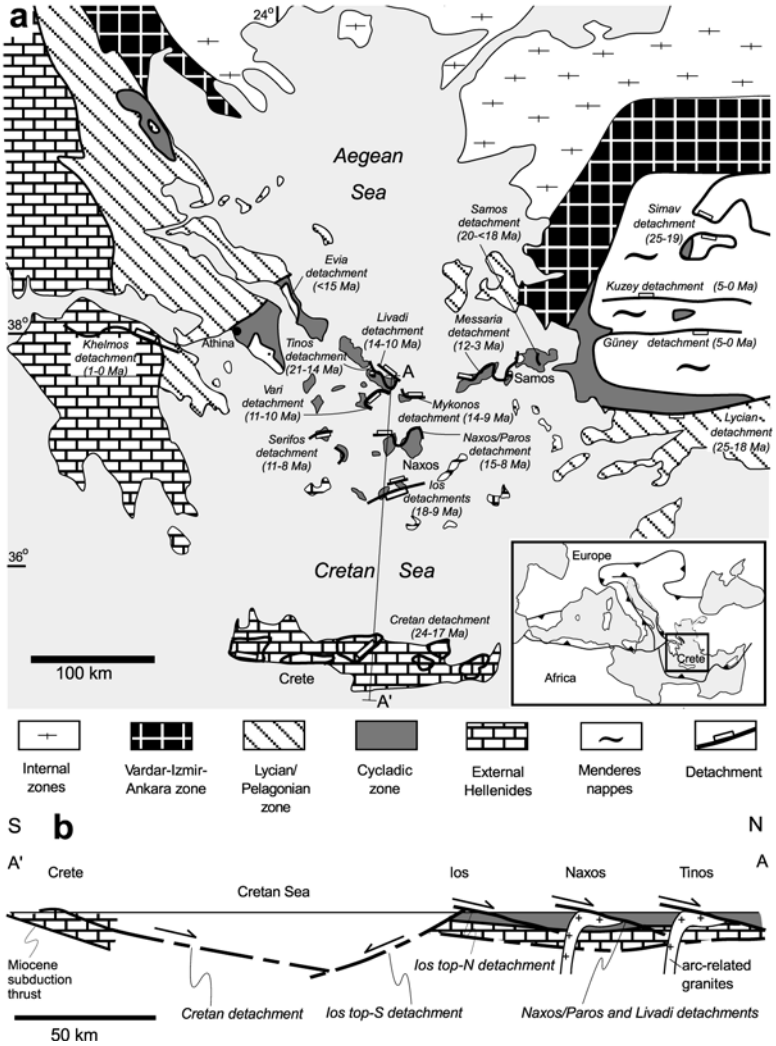

Figure 1. (a) Generalized tectonic map of Hellenides showing major tectonic zones and major Miocene to Recent extensional detachments with timing of slip (see *Brichau et al.* [2007] for summary of data). Insert shows Miocene to Recent thrust fronts in the Mediterranean and location of main map. (b) NNE-SSW cross section showing nappe pile and major Miocene detachments in the southern Aegean. Cretan detachment operated above early Miocene subduction thrust; Naxos and Livadi detachments are pretectonic to syntectonic to arc-related middle-late Miocene granites.

stratigraphy, tectonometamorphic history and preorogenic paleogeography [*Dürr et al.*, 1978; *Robertson et al.*, 1991]. The Cycladic zone is fringed to the north by the oceanic Vardar-Izmir-Ankara suture zone, and the continental Lycian/Pelagonian zone (Figure 1). The dominant tectonic unit of the Cycladic zone is the Cycladic blueschist unit, which comprises a Carboniferous basement at the base, a post-Carboniferous cover sequence and an ophiolitic mélange at the top. The Cycladic blueschist unit is overlain on some islands by the upper unit, which on the islands of Syros and Tinos is in turn overlain by the Vari/Akrotiri unit [*Patzak et al.*, 1994]. In a few windows in the Cycladic zone, the Basal unit, as part of the External Hellenides, crops out below the Cycladic blueschist unit [*Godfriaux*, 1968; *Avigad and Garfunkel*, 1989].

[6] The metamorphic evolution of the Cycladic blueschist unit involved an Eocene high-pressure event (15–20 kbar and 500–550°C on most islands) that commenced at ~55–50 Ma [*Tomaschek et al.*, 2003]. The exhumation of the Cycladic blueschist unit was diachroneous across the Cyclades and westernmost Turkey. Depending on its exhumation history, high-pressure metamorphism in the Cycladic blueschist unit lasted in some regions until ~40 Ma and in others until ~30 Ma [*Forster and Lister*, 1999; *Ring et al.*, 2007] and was followed by one or more greenschist- to amphibolite-facies overprints [*Wijbrans et al.*, 1990; *Ring and Layer*, 2003; *Schmädicke and Will*, 2003]. High-pressure metamorphism in the Basal unit (8–10 kbar and 350–400°C [*Shaked et al.*, 2000]) is dated at 24–21 Ma [*Ring et al.*, 2001; *Ring and Reischmann*, 2002].

[7] *Fytikas et al.* [1984] showed that the magmatic arc of the southward retreating Hellenic subduction zone shifted southward with time in the Tertiary. In the middle to late Miocene, that magmatic arc reached the Cyclades as evidenced by arc-related volcanic rocks ranging from ~12–5 Ma [*Fytikas et al.*, 1984; *Weidmann et al.*, 1984] and granites spanning an age range from ~15–10 Ma [*Keay*, 1998, *Brichau et al.*, 2007]. The granites are syntectonic to major extensional detachments [*Faure et al.*, 1991; *Lee and Lister*, 1992; *Lister and Forster*, 1996, *Kumerics et al.*, 2005].

2.1. Geology of Tinos Island

[8] The tectonostratigraphic framework of Tinos comprises four tectonic units (Figure 2), which are from bottom to top the Akrotiri unit, the upper unit, the Cycladic blueschist unit and the Basal unit. The Akrotiri unit consists of amphibolite and paragneiss which were metamorphosed at lower amphibolite-facies conditions (6.5–7.5 kbar and 530–610°C) [*Patzak et al.*, 1994]. Amphibole yielded hornblende K-Ar ages of 77–66 Ma, while muscovite from paragneiss gave K-Ar ages between 60 and 53 Ma [*Maluski et al.*, 1987; *Patzak et al.*, 1994]. The Akrotiri unit is separated from the underlying upper unit by the Vari detachment [*Ring et al.*, 2003a]. The upper unit comprises serpentinite, metagabbro, ophicalcite and phyllite [*Melidonis*, 1980]. A greenschist-facies metamorphic overprint occurred at ~21 Ma concurrent with top-to-the-NE extensional shearing on the Tinos detachment that underlies the upper unit [*Bröcker and Franz*, 1998; *Zeffren et al.*, 2005] (Figure 2). This greenschist-facies tectonometamorphic event has not been detected in the Akrotiri unit [*Patzak et al.*, 1994]. The Cycladic blueschist unit below the upper unit consists of marble, calcschist, mica schist, quartzite, metaconglomerate and metavolcanic rocks [*Melidonis*, 1980]. The Basal unit at the bottom of the succession comprises marble and minor metapelite [*Avigad and Garfunkel*, 1989]. The contact between the Cycladic blueschist unit and the Basal unit is not well known. At some stage in the late Oligocene this contact must have been a thrust putting the Cycladic blueschist unit above the Basal unit and causing high-pressure metamorphism in the latter [*Avigad and Garfunkel*, 1989; *Shaked et al.*, 2000; *Ring and Layer*, 2003; *Ring et al.*, 1999, 2007]. Northwest of Panormos (Figure 2), the Basal unit is in direct contact with the upper unit along the Tinos detachment and the entire Cycladic blueschist unit has been cut out in between.

[9] A large monzogranite intruded the Cycladic blueschist unit. At the periphery of the monzogranite, small leucogranites intruded the monzogranite and the Cycladic blueschist and upper units. One of leucogranites yielded a U-Pb zircon age of 14 Ma [*Keay*, 1998]. We refer to these granites collectively as the Tinos granites. The granites have a well-developed contact aureole that formed at ~14 Ma [*Bröcker and Franz*, 2000]. At ~12–11 Ma, a number of dacitic dikes intruded the basement of Tinos [*Avigad et al.*, 1998] (Figure 2). *Bröcker and Franz* [2000] reported Rb-Sr biotite ages of 10–8 Ma from the contact aureole of the Tinos granites.

2.2. Extensional Detachments on Tinos Island

[10] Usually one single extensional fault, the top-to-the-NE Tinos detachment at the base of the upper unit, is considered on Tinos Island [*Avigad and Garfunkel*, 1989; *Patriat and Jolivet*, 1998; *Zeffren et al.*, 2005; *Mehl et al.*, 2005]. In several places, the Tinos detachment is a sharp and striking contact decorated with a distinct, several meters thick layer of cataclasite [*Patriat and Jolivet*, 1998]. *Mehl et al.* [2005] mapped ductile and brittle structures associated with extensional deformation on Tinos and interpreted them to show a progressive structural evolution across the brittle-ductile transition zone and pronounced localization of extensional deformation on the Tinos detachment. If this view was right, then low-temperature cooling ages in the footwall of the Tinos detachment should get systematically younger northeastward in the direction of hanging wall slip and should display a fairly simple younging trend.

[11] Our observations show that there is a tens to more than 100-m-thick ductile shear zone below and above the Tinos detachment [see also *Zeffren et al.*, 2005]. In the Cycladic blueschist unit below the Tinos detachment, a prominent NE trending stretching lineation is developed (Figure 2) [see also *Patriat and Jolivet*, 1998; *Mehl et al.*, 2005]. This stretching lineation is expressed by aligned white mica and chlorite, as well as stretched calcite and quartz-albite aggregates. In the upper unit above the Tinos detachment, a similarly oriented stretching lineation is marked by the same minerals and also elongated epidote in greenschist. Shear sense indicators associated with this stretching lineation yield a consistent top-to-the-NE sense of shear [see also *Patriat and Jolivet*, 1998]. In the shear bands quartz is recrystallized and new chlorite and white mica grew. Greenschist-facies mylonitization along the Tinos detachment occurred at ~21 Ma (see above) and the detachment is cut by leucogranite at ~14 Ma [*Keay*, 1998] (Figure 2). As discussed above, in the northwestern part of the island, the Tinos detachment cuts down through the entire Cycladic blueschist unit and ultimately places the upper unit directly above the Basal unit. Stretching lineations and associated shear sense indicators in the Basal unit near Panormos (Figure 2) show the same direction, sense of shear and deformation/metamorphism relationships as the stretching lineation in the Cycladic blueschist unit and upper unit suggesting that the upper contact of the Basal unit is the Tinos detachment.

[12] *Ring et al.* [2003a] mapped the Vari detachment between the Akrotiri and the upper unit (Figures 2 and 3) in southern Tinos and argued that the Vari detachment reappears in the southeastern corner of adjacent Syros Island, where it is much better exposed. The fault zone of the Vari detachment is made up of brecciated cataclasite in which rocks from the hanging wall and footwall are intermixed. The rocks immediately above and especially below the Vari detachment are strongly cataclastically reworked and there is no pervasive ductile deformation associated with the Vari detachment. A NE trending stretching lineation (Figure 2) associated with brittle shear sense indicators indicates top-to-the-NE tectonic transport on the

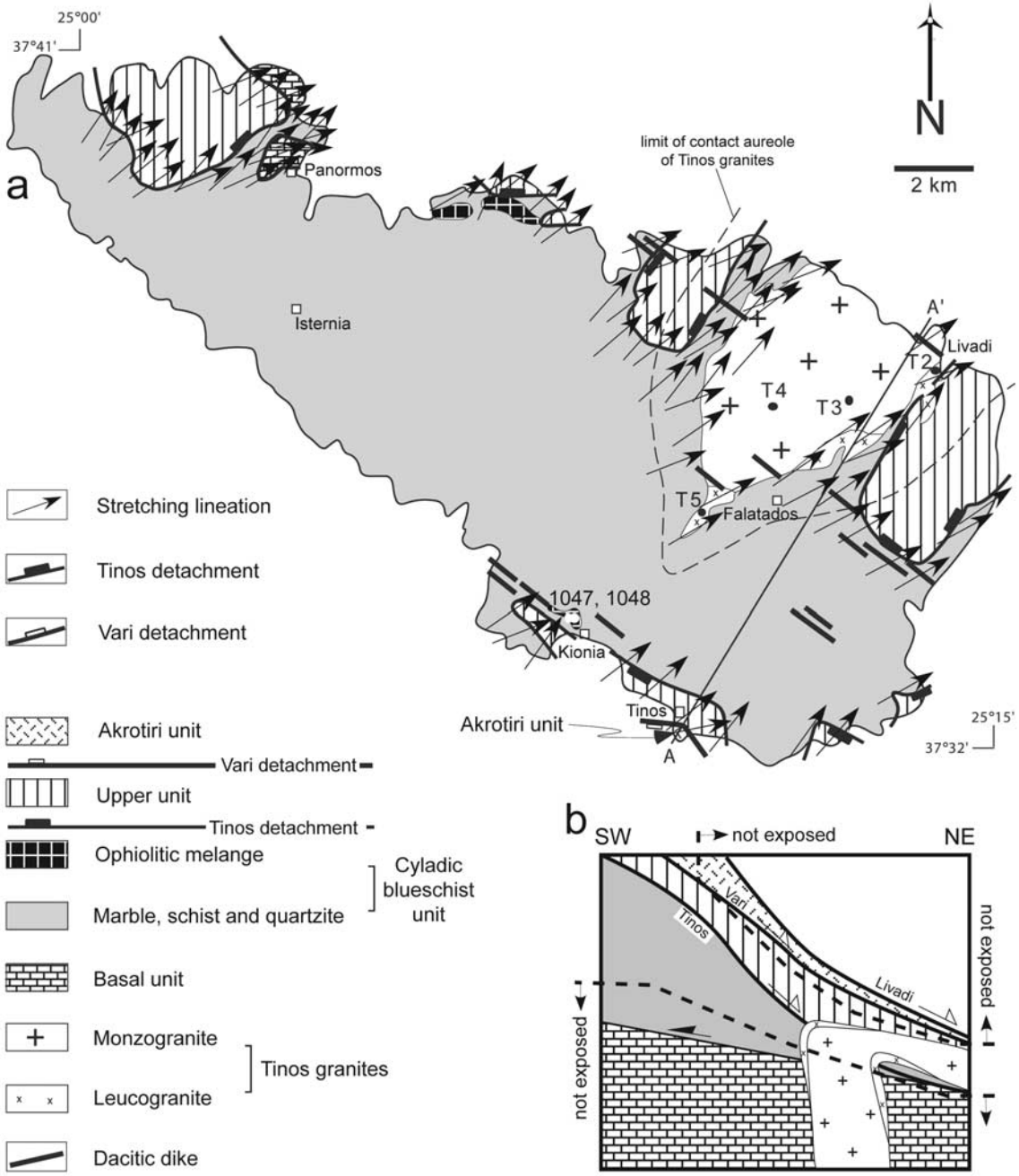

Figure 2. (a) Tectonic map of Tinos with Tinos and Vari detachments. Stretching lineations associated with various detachment and sample localities (T2, T3, T4, and T5 are from this study; 1047 and 1048 are from *Ring et al.* [2003a]) are also shown. Dacitic dikes are dated at ~12–11 Ma according to *Avigad et al.* [1998]. Note that Livadi detachment has not yet been mapped on Tinos and might have been eroded away. (b) Simplified and schematic diagram showing tectonostratigraphic units and Tinos, Vari, and Livadi detachments. Dashed lines indicate parts that are not exposed on Tinos Island.

detachment. Fission track dating by *Ring et al.* [2003a] showed that the Vari detachment operated at ~10 Ma on Tinos Island (note that deformation occurred earlier at ~11 Ma on Syros Island).

[13] Below we describe extensional structures in the Tinos granites. Because the granites stitch the Tinos detachment, these structures cannot be related to the latter. We will argue that the extensional structures in the Tinos granites are

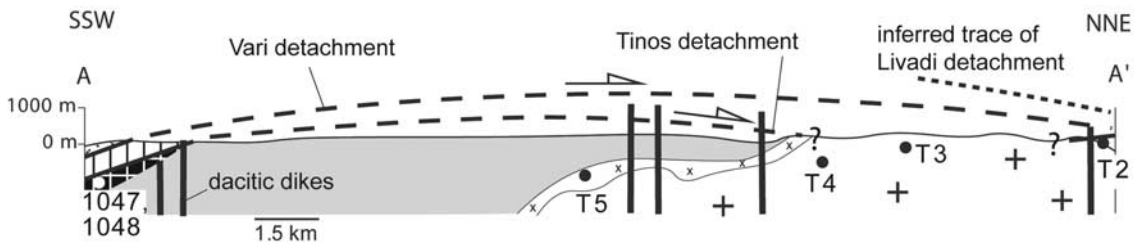

Figure 3. Schematic cross section showing tectonic units and sample localities. Greenschist-facies Tinos detachment between Cycladic blueschist unit and upper unit is dated at ~21 Ma [*Bröcker and Franz*, 1998]; 14 Ma old leucogranite pierces Tinos detachement; Vari detachment formed later than Tinos detachment and brought Akrotiri unit from SW into present position on Tinos Island; note that sample T2 is from leucogranite that stitched Tinos detachment. Livadi detachment might occur between Tinos and Vari detachment and/or structurally above both detachments (latter option is preferred interpretation, see text).

probably related to the Livadi detachment. Note that based on the data described below we infer the existence of Livadi detachment but this detachment is not exposed on Tinos island (Figure 3).

2.3. Previous Fission Track Dating

[14] *Altherr et al.* [1982] reported titanite and apatite fission track ages, determined by the population method, of 13.8 Ma and 10.8 Ma from the Tinos monzogranite. Using the same method, *Hejl et al.* [2002] reported four fission track ages ranging between 9.5 ± 0.8 Ma and 8.4 ± 0.7 Ma from the monzogranite and one age of 13.1 ± 4.4 Ma from the Cycladic blueschist unit.

[15] The population method for fission track dating demands a homogeneous uranium distribution in the dated minerals. *Hejl et al.* [2002] stated that the very low spontaneous track densities and rather homogenous uranium distribution in apatite guided them to use the population technique. However, our apatite fission track mounts from the Tinos monzogranite reveal enough spontaneous tracks for making the samples suitable for the Zeta method, which is the commonly used method in fission track dating [*Hurford and Green*, 1983]. Furthermore, a number of grains reveal a zonation of uranium, which is a problem for dating by the population method (Figure 4). Therefore neither the fission track ages of *Hejl et al.* [2002] nor those of *Altherr et al.* [1982] will be used in this study.

[16] *Ring et al.* [2003a] reported two consistent ZFT ages of 10.2 ± 1.2 Ma and 10.1 ± 0.7 Ma from the ophiolitic mélange near Kiona in southern Tinos (samples 1047 and 1048 in Figure 2). By combining data from Syros (mean ZFT age of 11.0 ± 0.4 Ma) and Tinos islands, *Ring et al.*

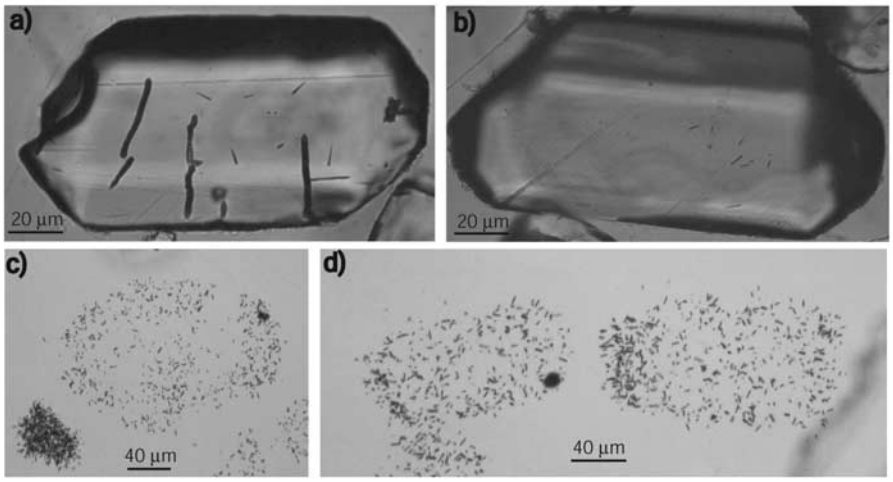

Figure 4. Microphotographs of fission track mounts showing zonation of uranium in apatite from monzogranite. (a) Sample T3 showing spontaneous fission tracks concentrated in core of apatite grain. (b) Spontaneous fission tracks in sample T4 concentrated in center of grain. (c) Heterogeneous reparation of induced tracks in mica from apatite of sample T3. (d) Induced tracks in mica showing higher concentration of tracks on left-hand side of apatite grain (sample T3).

Table 1. U-Th-Pb Isotope and Ti Concentration Data[a]

					Measured Isotope Ratios and 1σ Internal Errors, %								Corrected Ages and Absolute Internal Errors 1σ, Ma													
Analysis	Type	Pb,[b] ppm	U, ppm	Atomic Th/U	$^{206}Pb/^{238}U$	1σ ±	$^{207}Pb/^{235}U$	1σ ±	$^{207}Pb/^{206}Pb$	1σ ±	$^{208}Pb/^{232}Th$	1σ ±	$^{206}Pb^*/^{238}U$	1σ ±	$^{207}Pb^*/^{235}U$	1σ ±	$^{207}Pb^*/^{206}Pb^*$	1σ ±	Concordance, [c]%	Percent Common ^{206}Pb[c]	Spot MSWD[c]	Selected Age,[d] Ma	1σ Absolute External Error[d]	Ti, ppm	1σ ±[e]	Estimated T,[e] °C	1σ ±[e]
T3-01	core	3.33	1051	0.32	0.00287	2.3	0.07501	6.5	0.18928	6.1	0.00444	6.5	15.18	0.43	8.62	6.7	0.02	0.01	176	19.55	3.42	-	-	12.5	0.8	761	6
T3-02	rim	1.56	647	0.29	0.00241	1.3	0.01799	5.1	0.05420	4.9	0.00099	4.5	15.33	0.20	13.93	1.3	0.50	0.04	110	1.46	1.57	15.33	0.30	-	0.2	658	4
T3-03	core	1.24	511	0.27	0.00245	1.2	0.01570	6.6	0.04650	6.5	0.00089	3.9	15.71	0.18	14.11	1.2	0.39	0.03	111	0.59	5.00	-	-	4.9	0.5	694	7
T3-04	rim	2.04	900	0.43	0.00220	1.0	0.01359	4.7	0.04470	4.6	0.00070	2.9	14.26	0.14	13.70	1.0	1.50	0.11	104	0.00	1.06	14.26	0.25	5.0	0.2	683	3
T3-06	rim	3.56	1236	0.49	0.00237	1.7	0.03916	8.2	0.11982	8.0	0.00231	11.8	14.05	0.29	14.66	4.3	135.87	37.22	96	8.78	1.64	-	-	6.9	0.6	710	7
T3-07	core	1.07	378	0.38	0.00270	2.4	0.05072	7.9	0.13604	7.6	0.00217	7.6	15.63	0.41	14.11	5.1	0.52	0.17	111	11.48	5.00	-	-	4.8	0.3	680	5
T3-08	rim	11.47	5933	0.09	0.00207	1.6	0.01522	3.6	0.05338	3.2	0.00099	4.0	13.23	0.22	13.58	0.6	77.02	3.12	97	0.72	5.00	-	-	4.1	0.3	669	6
T3-09	core	1.42	620	0.32	0.00228	1.2	0.01589	6.5	0.05050	6.4	0.00085	4.0	14.63	0.19	13.74	1.3	0.86	0.08	107	0.84	1.16	14.63	0.28	3.3	0.2	651	4
T3-10	rim	1.74	788	0.20	0.00229	1.2	0.01619	5.8	0.05136	5.6	0.00076	5.2	14.74	0.18	15.96	1.1	209.00	13.07	92	0.13	1.42	14.74	0.28	bdl	-	-	-
T3-11	rim	1.38	585	0.42	0.00232	1.4	0.01461	5.9	0.04575	5.7	0.00069	3.6	15.02	0.22	15.56	1.3	108.85	8.21	97	−0.30	1.34	15.02	0.31	4.5	0.3	676	5
T3-12	core	0.97	434	0.33	0.00223	1.6	0.01501	6.7	0.04889	6.5	0.00080	5.2	14.27	0.24	12.98	1.4	0.49	0.05	110	0.82	1.49	14.27	0.32	4.0	0.2	666	4
T3-13	rim	2.31	1018	0.25	0.00231	1.1	0.01522	4.8	0.04781	4.7	0.00081	3.0	14.85	0.16	14.24	1.0	1.39	0.09	104	0.40	1.44	14.85	0.27	bdl	-	-	-
T3-14	rim	4.16	1990	0.10	0.00224	0.9	0.01448	3.3	0.04698	3.1	0.00069	4.8	14.42	0.13	14.81	0.5	79.11	2.57	97	−0.08	1.91	14.42	0.25	bdl	-	-	-
T3-15	rim	0.90	415	0.29	0.00220	1.8	0.01680	8.4	0.05546	8.2	0.00076	5.6	14.12	0.26	15.76	1.7	280.39	25.69	90	0.44	5.00	14.12	0.33	5.1	0.3	684	5
T3-17	core	2.47	1063	0.35	0.00230	1.1	0.01664	4.9	0.05242	4.8	0.00077	3.7	14.83	0.17	15.89	1.2	187.61	12.82	93	0.32	1.46	14.83	0.27	bdl	-	-	-
T3-19	core	0.43	178	0.29	0.00248	2.5	0.02720	15.9	0.07956	15.7	0.00073	11.6	16.04	0.41	27.82	4.5	1223.19	115.25	58	−0.20	5.00	-	-	4.6	0.3	677	5
T3-20	core	1.79	720	0.43	0.00236	1.3	0.02147	4.6	0.06606	4.4	0.00108	3.2	14.79	0.19	12.95	1.3	0.36	0.03	114	3.10	1.58	14.79	0.29	4.1	0.2	669	4
T3-21	core	1.57	663	0.35	0.00236	1.9	0.01564	7.9	0.04812	7.7	0.00075	5.3	15.21	0.30	15.40	1.6	51.76	5.18	99	0.13	5.00	15.21	0.37	3.6	0.3	658	6
T3-22	rim	1.83	784	0.35	0.00227	1.0	0.02306	5.8	0.07384	5.7	0.00116	4.9	14.16	0.16	14.03	1.7	13.27	1.59	101	3.41	5.00	14.16	0.26	5.8	0.3	695	4
T3-23	core	1.98	754	0.71	0.00229	1.6	0.03545	6.1	0.11229	5.9	0.00125	3.4	13.57	0.24	11.08	3.0	0.21	0.05	122	9.04	2.00	-	-	49.2	3.6	903	9
T3-24	core	2.34	1077	0.34	0.00215	1.3	0.01414	5.4	0.04780	5.3	0.00080	5.4	13.78	0.18	12.63	1.1	0.54	0.04	109	0.64	1.63	-	-	bdl	-	-	-

[a]Abbreviation bdl is below detection limit; concordance is based on agreement between $^{206}Pb^*/^{238}U$-$^{207}Pb^*/^{235}U$ ages; average crystallization temperature was calculated using underlined values.
[b]Radiogenic component only.
[c]Pooled age (N = 13; MSWD = 1.8; discordance limit = 1).
[d]Mean 14.63 ± 0.22 Ma (2σ).
[e]Mean 671 ± 14°C.

Table 2. The $^{40}Ar/^{39}Ar$ Hornblende Data

Step	$^{40}Ar^{*}/^{39}Ar$	$^{36}Ar/^{40}Ar \times 1000$ J = 0.011781	$^{39}Ar/^{40}Ar$	$^{37}Ar/^{39}Ar$	Percent ^{39}Ar	Percent Atmospheric	Age, Ma	Error 1σ
				T3 Amphibole[a]				
1	17.732	2.789	0.0099	6.911	0.0	82.4	342.28	159.51
2	8.817	2.643	0.0247	2.632	0.1	78.1	178.31	65.10
3	8.280	1.365	0.0719	1.524	0.3	40.3	167.93	23.00
4	1.886	1.888	0.2341	1.031	0.6	55.8	39.66	51.37
5	0.970	2.103	0.3898	1.827	0.9	62.1	20.51	27.46
6	0.932	0.715	0.8456	2.609	1.5	21.1	19.7	9.61
7	1.462	3.022	0.0731	3.253	1.7	89.3	30.82	57.31
8	1.183	1.955	0.3565	4.280	2.1	57.7	24.97	19.86
9	1.460	0.482	0.5871	4.194	2.6	14.2	30.78	12.11
10	0.586	1.584	0.9059	4.296	3.8	46.8	12.43	6.86
11	1.625	3.000	0.0697	2.565	4.6	88.6	34.23	18.86
12	1.078	0.064	0.9091	2.611	6.3	1.9	22.78	5.09
13	0.821	1.717	0.5996	3.006	20.2	50.7	17.36	0.73
14	0.783	0.126	1.2287	3.073	21.3	3.7	16.57	6.54
15	0.941	0.172	1.0086	3.863	22.1	5.0	19.89	10.96
16	0.660	1.209	0.9725	4.500	65.5	35.7	13.98	0.42
17	0.623	1.302	0.9855	4.500	87.2	38.5	13.21	0.56
18	0.637	1.032	1.0901	3.739	100.0	30.5	13.49	0.78
				T4 Amphibole[b]				
1	3.540	2.314	0.0892	1.668	1.6	68.3	73.72	4.16
2	1.544	1.527	0.355	1.083	4.7	45.1	32.54	2.26
3	0.951	1.434	0.6053	0.300	7.5	42.3	20.11	1.93
4	0.765	1.521	0.7187	0.163	9.8	44.9	16.19	2.42
5	0.859	1.074	0.7939	1.017	15.2	31.7	18.18	0.99
6	0.887	0.398	0.9944	1.001	20.6	11.7	18.75	1.30
7	0.706	0.829	1.0680	1.611	26.3	24.5	14.96	1.39
8	0.667	0.965	1.0700	2.270	35.1	28.5	14.13	0.93
9	0.662	1.106	1.0153	1.806	42.5	32.6	14.03	0.66
10	0.732	0.930	0.9900	1.661	48.7	27.4	15.50	1.00
11	0.651	0.971	1.0943	2.257	66.3	28.6	13.79	0.42
12	0.733	0.188	1.2866	2.294	69.1	5.5	15.53	1.86
13	0.743	0.434	1.1720	2.547	80.9	12.8	15.73	0.23
14	0.797	0.545	1.0519	2.180	100.0	16.1	16.87	0.39

[a]Total age is 15.5 ± 0.4 Ma.
[b]Total age is 17.1 ± 0.3 Ma.

[2003a] suggested a minimum time-averaged slip rate of ~6.5 km Ma^{-1} for the Vari detachment. They also showed that samples from the hanging wall (Vari unit) yielded older fission track ages (ZFT age of 20.4 ± 0.9 Ma and AFT age of 10.7 ± 5.5 Ma). The two ages reported by *Ring et al.* [2003a] were obtained by the Zeta method and can therefore by compared to the ages reported in this study.

3. Sampling and Methodology

[17] To calculate slip rates for the detachment above the Tinos granites, we collected samples from rocks in the footwall of the detachment along a profile parallel to the supposed tectonic transport direction on the fault (Figures 2 and 3). Before sampling we anticipated that the detachment above the granites is the Vari detachment of *Ring et al.* [2003b]. However, the age data reported below are at variance with this assumption; therefore we refer to the detachment that caused tectonic cooling of the granites as the Livadi detachment. The Livadi detachment is not shown in Figure 2 and schematically sketched in Figure 3 because the detachment has so far not been mapped on Tinos and most probably has been eroded away.

[18] Samples T2 and T5 are from leucogranite and samples T3 and T4 are from the monzogranite. Sample T2 is from a leucogranite at the northern coast and was taken structurally directly below the Tinos detachment. However, this leucogranite intruded the Tinos detachment some tens of meters structurally above the T2 sample locality. We report U-Pb zircon, $^{40}Ar/^{39}Ar$ hornblende and zircon and apatite fission track and (U-Th)/He ages (Tables 1–4). All errors are quoted to the 2σ level, except the $^{40}Ar/^{39}Ar$ ages, which are quoted to the 1σ level.

3.1. U-Pb Dating and Ti Abundance Measurements

[19] The only U-Pb zircon age from the Tinos granites is that of 14.4 ± 0.2 Ma from a leucogranite [*Keay*, 1998]. We analyzed zircons from sample T3 for constraining the intrusion age of the monzogranite. The zircons were hand-picked, mounted in epoxy, polished and analyzed by exci-

Table 3. Zircon and Apatite Fission Track Data[a]

Sample Reference (Rock Type)	Latitude, Longitude	Elevation, m	Distance in Slip Direction, km	Mineral	Number of Crystals	Track Density, × 10^6 trace cm^{-2}					FT Age, Ma	Mean Track Length, μm	SD, μm	Number of Tracks Measured
						ρd [Nd]	ρi [Ni]	ρs [Ns]	Pχ^2, %	U, ppm				
T2 (granodiorite)	37°36′39″, 25°14′08″	0	0.76 ± 1	apatite	30	1.528 [13182]	0.9193 [139]	1.91 [2888]	97.1	15.6	11.9 ± 2.0	14.8 ± 0.3	1.2	58
				zircon	11	0.38 [4911]	33.15 [1137]	6.563 [2251]	83.3	633.8	12.2 ± 1.0			
T3 (granodiorite)	37°36′19″, 25°12′17″	340	2.98 ± 1	apatite	21	1.3552 [10618]	0.6369 [100]	1.142 [1793]	98.4	10.5	12.6 ± 2.6	14.2 ± 0.4	1.1	37
				zircon	13	0.37 [4911]	43.07 [1710]	7.61 [3021]	96.8	754.8	13.3 ± 0.8			
T4 (granodiorite)	37°35′46″, 25°11′45″	465	4.22 ± 1	apatite	23	1.3472 [10618]	0.8735 [134]	1.529 [2345]	63.8	14.2	12.8 ± 2.4			
				zircon	15	0.365 [4911]	32.08 [1360]	5.408 [2293]	96.2	543.8	13.8 ± 1.0			
T5 (S-type granite)	37°34′35″, 25°09′39″	300	6.60 ± 1	zircon	12	0.358 [4911]	32.02 [1188]	5.075 [1883]	100	520.3	14.4 ± 1.2			

[a]Zircon and apatite fission track ages were calculated using zeta factors of 127 ± 4 and 330 ± 8.5 determined by multiple analyses of standards following recommendations of *Hurford and Green* [1983]; central ages are reported; data are quoted to 2σ level. Distance in fault slip direction for each individual sample has been measured from the northeast end of Tinos island. Although absolute geographic sample location errors are ±5 m, we adopted conservative distance uncertainties of 1 km (2σ) to encompass errors in determination of map distance in the slip direction, distance below the detachment surface, and lack of knowledge about possible intervening structures, and the changes in relative sample positions during the transition across the "rolling hinge" from dipping along the detachment at depth to being at roughly equivalent elevation today.

mer laser ablation (ELA-ICP-MS) following procedures reported by *Ballard et al.* [2001]. Data for mass peaks were collected in time-resolved mode with one point per peak. Because of a relatively high ^{204}Hg blank, ^{204}Pb was excluded. Integration times were: 40 ms for ^{206}Pb, ^{207}Pb, ^{208}Pb, ^{232}Th, ^{235}U, ^{238}U; 10 ms for ^{31}P; 5 ms for ^{29}Si, ^{91}Zr and 20 ms for ^{49}Ti. Following background substraction and rejection of outliers, instrumental mass bias and depth-related elemental fractionation were corrected for each spot analysis. Measured ^{207}Pb/^{206}Pb, ^{206}Pb/^{238}U, and ^{208}Pb/^{232}Th ratios in the standard zircon TEMORA and ^{232}Th/^{238}U in the silicate glass standard NIST610 were averaged over the course of each analytical session and used to calculate correction factors based on accepted values [*Pearce et al.*, 1997; *Black et al.*, 2003]. Pooled ^{206}Pb/^{238}U ages and associated errors include within session analytical error, external uncertainties in the analysis and age calibration of the zircon standard [*Stern and Amelin*, 2003]. Within session error was esti-

Table 4. Zircon and Apatite (U-Th)/He) Data

Sample	Mineral	n	He, nmol/g	U, ppm	Th, ppm	F_T	He Age, Ma	SD
T2	apatite	4	0.494	11.9	22.3	0.66	8.1 ± 0.5	
	apatite	4	0.741	11.4	22.0	0.74	11.2 ± 0.7	
	apatite	4	0.907	16.6	27.67	0.68	10.6 ± 0.6	
Mean			0.714	13.3	24.0	0.69	10.0 ± 0.3	1.6
	zircon	1	26.4	709.9	203.3	0.73	8.8 ± 0.7	
	zircon	1	130.6	3446.6	629.7	0.67	9.9 ± 0.8	
	zircon	1	43.5	1258.6	346.5	0.65	9.2 ± 0.7	
	zircon	1	50.9	1382.8	501.9	0.71	8.7 ± 0.7	
Mean			62.8	1699.5	420.3	0.69	9.2 ± 0.4	0.5
T3	apatite	4	0.620	12.1	19.8	0.69	9.9 ± 0.6	
	apatite	4	0.671	12.8	21.4	0.64	10.8± 0.6	
Mean			0.646	12.5	20.6	0.67	10.4 ± 0.4	0.6
T4	apatite	4	0.596	11.0	15.6	0.66	11.3 ± 0.7	
	apatite	4	0.774	11.8	19.1	0.70	12.5 ± 0.8	
Mean			0.685	11.4	17.4	0.68	11.9 ± 0.5	0.8
	zircon	1	15.2	288.6	86.9	0.71	12.8 ± 1.0	
	zircon	1	21.1	532.9	137.2	0.70	9.8 ± 0.8	
	zircon	1	15.5	337.1	111.2	0.68	11.6 ± 0.9	
	zircon	1	8.2	203.3	68.2	0.72	9.7 ± 0.8	
	zircon	1	30.8	759.3	120.4	0.76	9.5 ± 0.7	
	zircon	1	39.2	889.1	140.7	0.73	10.7 ± 0.9	
Mean			21.7	501.7	110.8	0.72	10.7 ± 0.3	1.3

mated using the standard deviation of $^{207}Pb/^{238}U$ measurements of NIST610 silicate glass. External errors incorporated only the uncertainty in the analysis of TEMORA, here taken as the standard error in the $^{206}Pb/^{238}U$ measurements [*Black et al.*, 2003].

[20] Common Pb corrections were applied based on the difference between measured and expected $^{208}Pb/^{206}Pb$ ratios for the measured $^{232}Th/^{238}U$ value, according to methods described by *Compston et al.* [1984]. Internal errors for individual analyses were calculated from the observed variation in the corrected isotope ratios for each mass scan over the data interval selected for age calculation. Analyses with resolvable isotopic heterogeneity (internal MSWD >3) were mostly rejected from further consideration. Concordance was calculated on the basis of agreement between $^{207}Pb/^{235}U$ and $^{206}Pb/^{238}U$ ages. Pooled $^{206}Pb/^{238}U$ ages and associated errors took into account within session analytical error, external uncertainties in the analysis, and age calibration of the zircon standard [*Stern and Amelin*, 2003]. Within session error was estimated using the standard deviation of $^{206}Pb/^{238}U$ measurements of NIST610 silicate glass. External errors incorporated only the uncertainty in the analysis of TEMORA, here taken as the standard error in the $^{206}Pb/^{238}U$ measurements, as the reported error in the age is negligible [*Black et al.*, 2003].

[21] *Watson et al.* [2006] have recently devised a thermometer, based on the temperature dependant incorporation of Ti^{4+} into crystallizing zircon under TiO_2-saturated conditions (i.e., rutile is present). Given petrographic evidence for the presence of rutile in sample T3 and using Ti concentrations obtained by LA-ICP-MS, $T_{crystallization}$ was calculated according to: $T\,[°C] = ((5080 \pm 30)/(6.01 \pm 0.03) - (\log(Ti)) - 273$ [*Watson et al.*, 2006, equation 7]).

3.2. The $^{40}Ar/^{39}Ar$ Dating

[22] The dating has been applied to hornblende separated under the binocular after coarse rock crushing and cleaning in ethanol and distilled water. All crystals were packed in aluminum foil and irradiated for 70 hours in the McMaster reactor (Canada) with MMHb hornblende neutron flux monitor dated at 520.4 ± 1.7 Ma [*Samson and Alexander*, 1987]. After irradiation, the single grains were placed on a Cu holder inside an UHV gas extraction system and baked for 48 hours at 200°C to clean the holder and extract the atmospheric argon potentially retained on the grain surface. For each selected sample, single grains of hornblende were analyzed, using a laser probe running in the continuous mode to extract the argon by step heating. The analytical device consists of (1) a multiline continuous 6 W argon ion laser; (2) a beam shutter for selection of exposure times, typically 30s for individual steps; (3) divergent and convergent lenses for definition of the beam diameter; (4) a small inlet line for the extraction and purification of gases; and (5) a MAP 215–50 noble gas mass spectrometer. Each analysis involved 5 min for lasering and gas cleaning and 15 min for data acquisition by peak switching from mass 40 to 36, through 10 sets of data. System blanks were evaluated every three analyses and range around 2×10^{-12} cm^3 for ^{40}Ar and 3×10^{-14} cm^3 for ^{36}Ar. For each analysis, standard isotope corrections were applied including blanks, mass discrimination radioactive decay of ^{37}Ar and ^{39}Ar and irradiation-induced mass interference.

[23] *Villa* [1998] and *Coulson et al.* [2002] showed that for rapidly cooling granites the closure temperature for Ar diffusion in large undeformed magmatic hornblende crystals is relatively high and we consider a closure temperature of 525 ± 50°C as shown by hydrothermal Ar bulk loss experiments [*Dahl*, 1996].

3.3. Fission Track Dating

[24] Samples for fission track analysis were irradiated with muscovite external detectors and Corning dosimeter glass CN-5 and CN-2 at the Radiation Center Oregon State University, which has a Cd/Au ratio >400. Fission track densities were measured using an optical microscope at 1250x magnification. Ages were calibrated by the Zeta method [*Hurford and Green*, 1983] using a zeta factor of 127 ± 4 and 330 ± 8.5, respectively, determined by multiple analyses of zircon and apatite age standards following the recommendations of *Hurford* [1990]. Ages were calculated using the central age method of *Galbraith and Laslett* [1993] which allows for non-Poissonian variation within a population of single-grain ages belonging to an individual sample. The χ^2 test indicates the probability that all grains counted belong to a single population of ages, a probability of less than 5% is taken as evidence for a significant spread of single grain ages. A spread in individual grain ages can result either from inheritance of detrital grains from mixed source areas, or from differential annealing in grains of different composition by heating within a narrow range of temperatures [*Green et al.*, 1989].

[25] Fission tracks in both apatite and zircon shorten or anneal with increased temperature and duration of heating. For apatite of typical Durango composition (0.4 wt % Cl) experimental and borehole data [*Green et al.*, 1989; *Ketcham et al.*, 1999] show that over geologic time fission tracks begin to anneal at a sufficient rate to be measurable above ~60°C, with complete annealing and total resetting of the apatite fission track age occurring between 100 and 120°C. This range of temperatures is usually labeled the apatite fission track partial annealing zone. For samples that have undergone moderate to fast cooling, a value of 100 ± 20°C is regarded as the closure temperature of fission tracks in apatite. In zircon, tracks are stable to higher temperatures. For pristine zircon, annealing over geologic time begins at 250 ± 20°C, with total resetting occurring above 310 ± 20°C [*Tagami et al.*, 1998], although these temperatures are lower in zircons with high accumulated radiation damage [*Rahn et al.*, 2004]. This translates into a closure temperature for fission tracks in zircon at moderate to fast cooling rates of 280 ± 30°C, which correlates well with the brittle-ductile transition [*Stöckhert et al.*, 1999].

[26] The number of measurable track lengths of the samples in this study was generally low due to a combination of young fission track age and low uranium concentration. For this reason, additional sample mounts were prepared for ^{252}Cf irradiation. This involves irradiating the samples with a collimated beam of heavy ions (^{252}Cf-

Table 5. Slip Rate Data[a]

Method	Samples	Slip Rate	Positive Error	Negative Error	MSWD	Probability of Fit	Average	Positive Error	Negative Error
Hbl Ar/Ar	T3 and T4	1.8	3.8	1.2	0	1	-	-	-
ZFT	T2 to T5	2.6	5.9	1.1	0.14	0.87			
ZHe	T2 and T4	2.3	2.5	0.8	0	1			
AFT	T2 to T4	3.7	5.4	2.8	0.01	0.94	2.6[b]	3.3[b]	1.0[b]
AHe[1c]	T2 to T4	1.7	2.1	1.5	3.86	0.05			
AHe[2d]	T2 to T4	1.5	5.6	0.6	1.68	0.19			

[a]Slip rates are in (km Ma^{-1}) and quoted to 2σ level.
[b]Average slip rate calculated with ZFT, AFT and AHe[2]. Hbl, hornblende; ZFT, zircon fission track; ZHe, zircon (U-Th)/He; AFT, apatite fission track; AHe, apatite (U-Th)/He.
[c]Slip rate estimated using the 6% error of the ages at 2σ.
[d]Slip rate estimated using the standard deviation as error on the ages.

derived fission fragments) for 24 hours [*Donelick and Miller*, 1991]. The exposures were made under vacuum to enable the neutrons to penetrate deeper into the apatite grains increasing the number of intersections with natural confined spontaneous tracks. Comparison of nonirradiated and Cf-irradiated aliquots suggest an overall deviation of ~3%, not exceeding that found for replicate analysis by a single analyst [*Barbarand et al.*, 2003].

3.4. (U-Th)/He Dating

[27] He, U and Th determinations are made on a single aliquot of one zircon and four apatite grains, typically 100 μm in minimum dimension. Extracted He was spiked with ^{3}He, cryogenically concentrated and purified, and the ^{4}He/^{3}He ratio determined using a quadrupole mass spectrometer after quantitative He degassing of zircon at 1300°C and apatite at 1050°C with a Nd-YAG laser for 10 and 5 min, respectively [*House et al.*, 2000]. Grains were retrieved from the vacuum system, dissolved in HF and HNO_3 for zircon and HNO_3 for apatite, spiked with ^{230}Th and ^{235}U, and analyzed for U and Th by Inductively Coupled Plasma Mass Spectrometry. Reported He ages are corrected for alpha ejection effects based on measured grain dimensions [*Farley et al.*, 1996]. Ages were replicated and the mean is reported. The estimated analytical uncertainties for zircon and apatite He ages are about 8% and 6% (2σ), respectively, according to laboratory internal reproducibility. Laboratory diffusion experiments and empirical calibration studies indicate that helium is partially retained at temperatures between ~190–120°C for zircon [*Reiners*, 2005] and ~80–40°C for apatite [*Stockli et al.*, 2000]; temperature intervals termed the partial retention zone.

3.5. Slip Rates

[28] Time-averaged slip rates were estimated by fitting a line to the age/distance data. The fitting procedure incorporates both measured age uncertainties and an estimated uncertainty of 1 km (2σ) in distance. Uncertainties were estimated using methods of *York* [1969] for noncorrelated errors. To estimate if the slip rates obtained are realistic compared to the scatter of the points and their assigned errors, the mean square of weighted deviates (MSWD) and probabilities of fit are indicated in Table 5. The MSWD is a measure of the ratio of the observed scatter of the points from the best fit line to the expected scatter from the assigned error. The probability of fit tests the assumption that the assigned errors are the only reason the data points scatter from a straight line. Therefore, if the probability of fit is >0.15 this assumption is considered justified [*Ludwig*, 2003]. In addition to estimate slip rates for individual thermochronometers, we combined multiple thermochronometers to obtain an overall time-averaged slip rate for the Livadi detachment.

4. Field Relationships and Synkinematic Emplacement of the Tinos Granites

[29] The large body of granite in the footwall of the Tinos detachment is mainly a medium- to coarse-grained amphibole-bearing monzogranite, whereas the small granite outcrops surrounding the monzogranite are made up of fine-grained garnet-bearing leucogranite [*Bröcker and Franz*, 2000]. The monzogranite is elongated in the NE direction. Large parts of the monzogranite are undeformed and exhibit magmatic textures [*Faure et al.*, 1991]. Relatively weakly aligned igneous minerals of euhedral potassium feldspar, plagioclase, biotite and hornblende and undeformed quartz define a magmatic foliation. Thin section work shows that the minerals forming the magmatic foliation do not show any signs of deformation or recrystallization. At the top of the monzogranite, the dip of the magmatic foliation is moderate to subhorizontal and the long axes of prismatic potassium feldspar occasionally are weakly aligned in a NE direction.

[30] In its margins, mainly in the west, the monzogranite locally shows a subhorizontal tectonic foliation associated with a relatively weakly expressed NE trending stretching lineation (Figure 2) defined by medium- to fine-grained flattened and elongated quartz grains and aligned biotite. Quartz forms polycrystalline ribbons (Figures 5a and 5b) shows undulated extinction, dynamic recrystallization and grain boundary migration. The ductile deformation structures show a progressive evolution into semiductile and brittle structures and potassium feldspar porphyroclasts and hornblende show brittle micronormal faults at moderate to high angle to the tectonic foliation. At its margins, the monzogranite is increasingly brecciated and fractured and

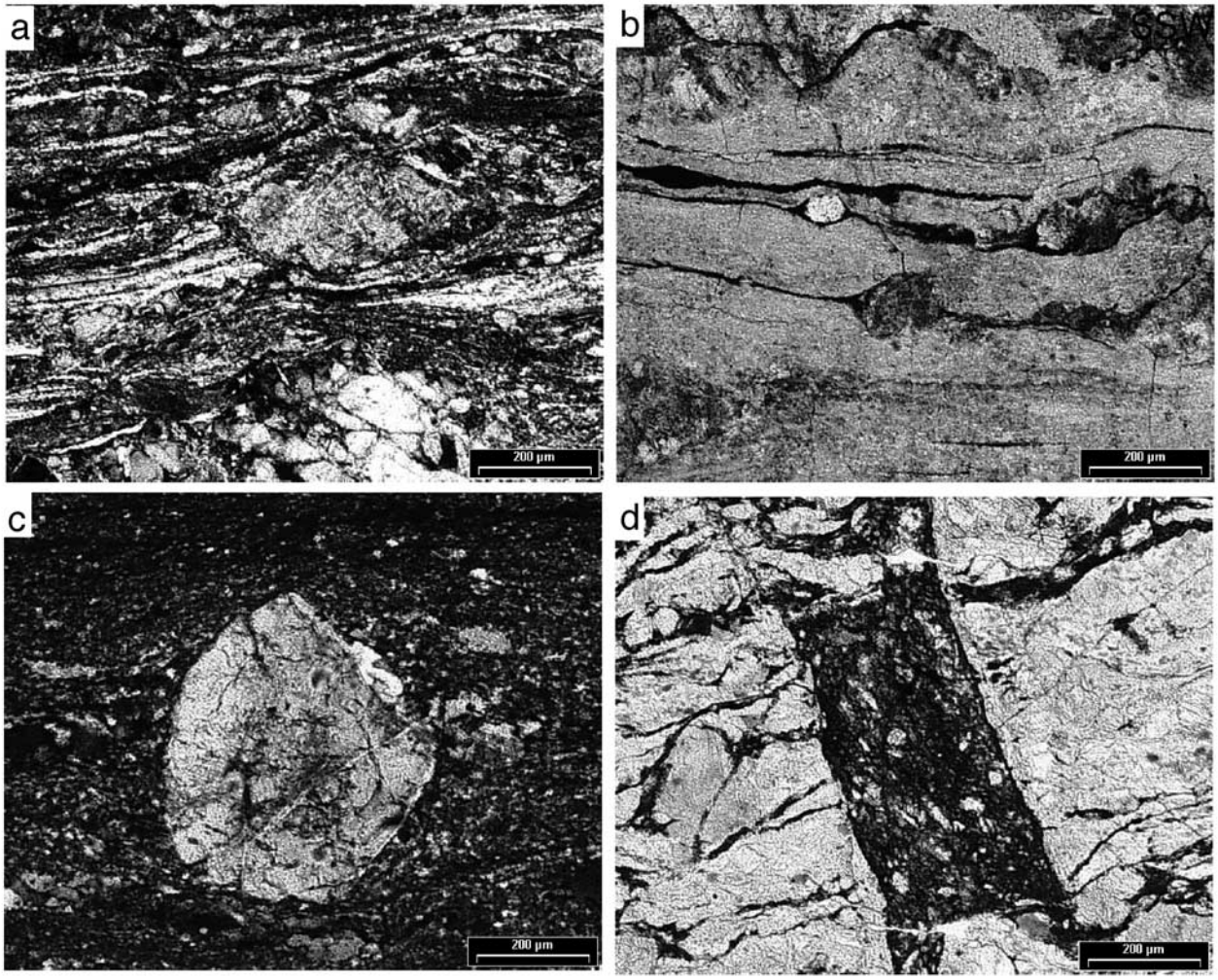

Figure 5. Microphotographs of deformed Tinos granites. (a) Narrowly spaced tectonic foliation in quartz-rich layers wrapping around seriticized feldspar porphyroclasts. (b) Ultrafine-grained quartz ribbons surrounding strongly seriticized feldspar porphyroclasts. (c) Leucogranite with cataclastic foliation wrapping around seriticized feldspar porphyroclast. (d) Brecciated vein cutting through mylonitic quartz-rich layers in leucogranite.

forms cataclasite (Figures 5c and 5d); occasionally, pseudotachylite occurs. Very fine-grained retrograde chlorite is common in the breccia zones and feldspar is severely altered to sericite. Rare shear bands, S-C fabrics, oblique quartz grain shape foliations, asymmetric biotite fish and Riedel structures indicate a top-to-the-NE shear sense.

[31] Most leucogranite is more strongly deformed than the monzogranite. A few leucogranite dikes cut across the mylonitic/cataclastic Tinos detachment near Livadi (Figure 2). The leucogranite has a tectonic foliation associated with a NE trending stretching lineation. The foliation is defined by flattened and elongated quartz and the lineation is expressed by stretched quartz aggregates and aligned muscovite. Feldspar porphyroclasts are not ductilely deformed and locally altered to sericite. Quartz forms polycrystalline ribbons and undulated extinction, dynamic recrystallization and grain boundary migration are common.

[32] The rocks in the contact aureole of the granites are commonly more deformed than the granites itself. Especially at the western margin of the granites, mica schist is severely deformed. *Bröcker and Franz* [2000] reported abundant contact metamorphic biotite in these rocks and this biotite is usually kinked. Top-to-NE displacing Riedel shears grade into small-scale top-to-NE displacing normal faults at the western margin. The rather brittle style of deformation and deformation/metamorphism relationships of the extensional structures in the contact aureole at the western margin of the Tinos granites are different from those in the ductile shear zone below the Tinos detachment.

[33] *Bröcker and Franz* [2000] dated contact metamorphic biotite by the Rb-Sr method at 10–8 Ma. Because the rocks in the contact aureole are strongly deformed, this deformation had an impact on the Rb-Sr system of the biotite and probably did reset it. Because of its low closure

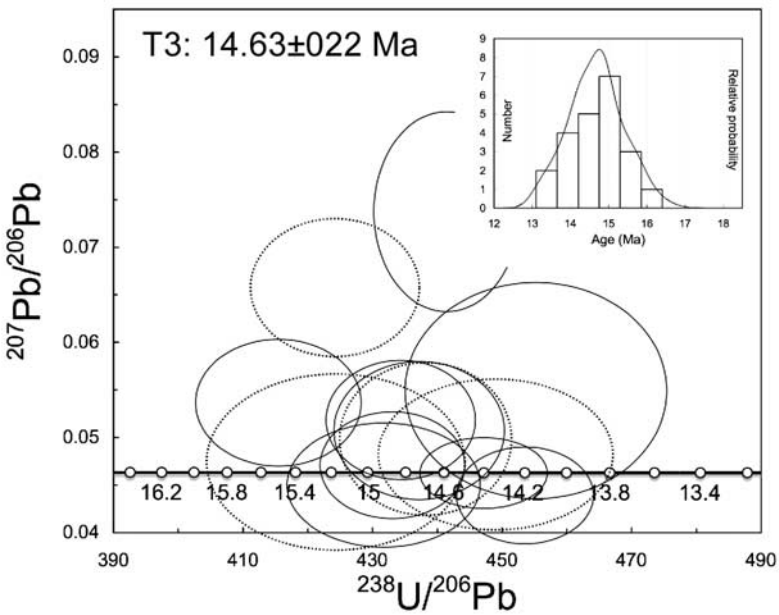

Figure 6. Tera-Wasserburg concordia diagram for common Pb-uncorrected U-Pb isotope data used to calculate $^{238}U/^{206}Pb$ age for sample T3. Cores are shown as dashed ellipses, rims are shown as continuous ellipses; data error point ellipses are 1σ. Inset shows cumulative probability plot of all 21 spot analyses and superimposed histogram (bin width 0.5 Ma).

temperature, biotite is known to be very reactive, and even the slightest alteration has a pronounced effect on the biotite and usually resets its radiometric age [*Clauer et al.*, 1982]. Therefore we concur with *Bröcker and Franz* [2000], who proposed that the Rb-Sr biotite ages of 10–8 Ma are most likely related to postintrusion deformation at the margin of the granites. This interpretation is in line with the different deformation style of the extensional structures at the western margin of the granites.

5. Age Data

[34] The U-Pb zircon data are reported in Table 1, the $^{40}Ar/^{39}Ar$ hornblende data in Table 2 and the zircon and apatite fission track and (U-Th)/He data in Tables 3 and 4.

5.1. U-Pb Dating and Ti_{zircon} Thermometry

[35] Twenty-one zircon grains were imaged by CL and analyzed for U-Pb-Th isotope ratios and Ti concentrations. The zircons range in size from 150 to 350 μm (long axis) and are generally prismatic, with aspect ratios of 3–6. Under CL the crystals are composed of elongate, homogeneous and irregularly zoned cores mantled by finely oscillatory-zoned rims. Mineral inclusions of apatite are common. The cores, most of which are concordant (Figure 6), yield $^{206}Pb/^{238}U$ ages ranging from 15.2 to 13.6 Ma. Oscillatory-zoned rims, interpreted here as crystallization products from igneous melts, produce a narrow age range of 15.3–13.2 Ma, which is indistinguishable from dates obtained for the cores. The distinct similarity in age, Th/U ratios of 0.3–0.4 and absolute concentrations of U and Pb strongly suggest that the rims and the cores were formed during the same crystallization event. When combined, the cores and rims yielded a $^{206}Pb/^{238}U$ age of 14.6 ± 0.2 Ma (N = 13, MSWD = 1.8, 2σ error). This age is indistinguishable within error to the age of 14.4 ± 0.2 Ma from the leucogranite sample dated by *Keay* [1998].

[36] Crystallization temperatures calculated for 15 zircons define a narrow range of 651–710°C, with one outlier of 903°C. The average $T_{crystallization}$ for 15 zircons used for U-Pb age determination is 671 ± 14°C (2σ). Uncertainty pertinent to calculating $T_{crystallization}$ with the Ti-in-zircon thermometer has been estimated by *Watson et al.* [2006] at ±8°C (2σ) for the temperature range observed in this study. Uncertainty arising from LA-ICM-MS analysis of Ti concentrations translates into a temperature range of 3–9°C. Both errors are smaller than the standard deviation for the arithmetic average.

5.2. The $^{40}Ar/^{39}Ar$ Dating

[37] The age spectra and Ca/K profiles for samples T3 and T4 are similar (Figure 7). Most of the incremental heating experiments resulted in relatively flat spectra with excess argon in the lower-temperature steps leading to high apparent ages which step down at ~20% of released ^{39}Ar for both samples. Sample T3 yields a well-defined plateau age of 13.7 ± 0.4 Ma for 78% of the released ^{39}Ar. Sample T4 has a slightly irregular saddle-shaped spectrum. The initial argon release yields old apparent ages which decrease with progressive ^{39}Ar release, defining a reasonably well-defined plateau age of 14.4 ± 0.4 Ma for 49% of the released ^{39}Ar. At the end of the spectrum the age seems

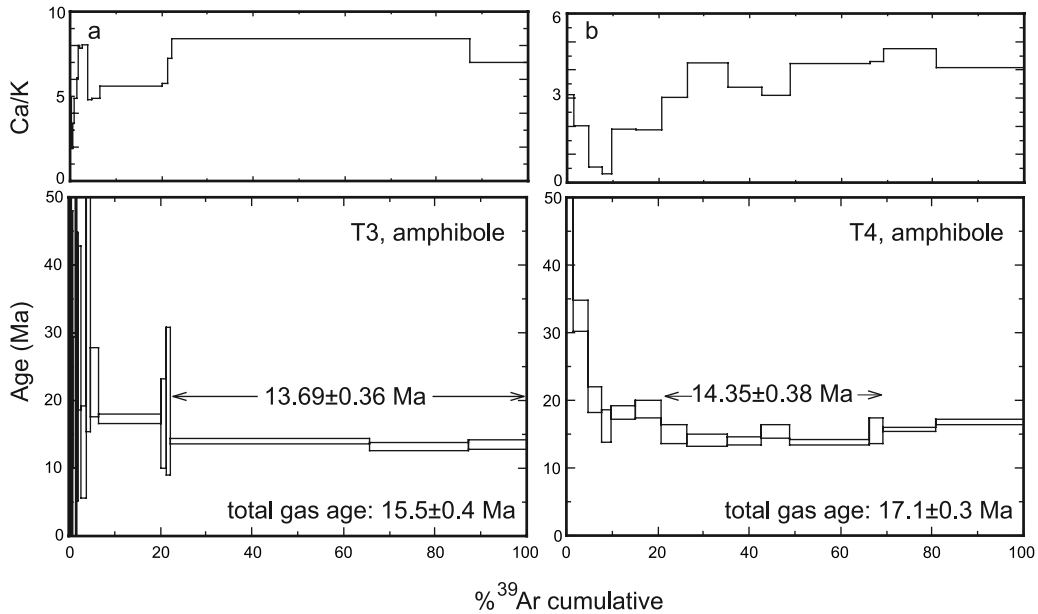

Figure 7. Results of $^{40}Ar/^{39}Ar$ dating on hornblende from samples T3 and T4. All age spectra and Ca/K profiles are shown with 1σ analytical error.

to become slightly older again. Recent data suggest that fluid inclusions, released at low temperature, and solid inclusions, released at high temperature during the experiment, are the most likely explanation [*Esser et al.*, 1997; *Boven et al.*, 2001; *Kelley*, 2002]. Ca/K profiles reflect a homogeneous argon source, with Ca/K values typical for Ca-amphiboles (>3).

5.3. Fission Track Dating

[38] The ZFT ages range between 14.4 ± 1.2 Ma and 12.2 ± 1.0 Ma and the AFT ages from 12.8 ± 2.4 Ma to 11.9 ± 2.0 Ma. All ages pass the χ^2 test at the 5% level, indicating that the single grain ages used to calculate the central age were derived from one age population [*Galbraith and Laslett*, 1993]. Apatite track length analyses, with 58 and 37 measured tracks, were obtained from two samples. The mean AFT track lengths are 14.2 ± 0.4 μm and 14.8 ± 0.3 μm, with low standard deviations (<1.2 μm), typical for samples that cooled quickly through the AFT partial annealing zone from ~110°C to below ~60°C at about the time represented by the AFT age [*Green et al.*, 1989].

5.4. (U-Th)/He Dating

[39] To provide an independent constraint for the ZFT and AFT results and to supply more precise lower-temperature thermochronologic constraints, ZHe and AHe age analyses were performed on selected samples. The three analytically acceptable AHe ages from the Tinos granites range from 11.9 ± 0.5 Ma to 10.0 ± 0.3 Ma, while the ZHe ages are 10.7 ± 0.3 Ma and 9.2 ± 0.4 Ma. Replicate analyses from the samples are usually similar within error providing added confidence in the AHe and ZHe ages.

[40] The ZHe ages are younger than the AFT and AHe ages, a feature that has also been reported from other Cycladic islands [*Brichau et al.*, 2006, 2007]. The anomalously young ZHe ages might be explained by U and Th zoning, as the zircon fission track mounts show thin, but highly U-enriched rims. Therefore a traditional F_T correction assuming homogeneous U and Th distribution would lead to an underestimation of the F_T correction and consequently of our ZHe ages [*Hourigan et al.*, 2005; *Reiners*, 2005].

6. Slip Rates and Cooling Paths

[41] The different data sets obtained from the various methods give internally consistent results that systematically decrease northeastward in the direction of hanging wall transport on the Livadi detachment. This decrease in ages reflects the lateral passage of isotherms at the top of the footwall and can be used to estimate a slip rate from the inverse slope of mineral ages with distance in the slip direction [*Foster and John*, 1999; *Stockli*, 2005]. The data yield minimum slip rates for the Livadi detachment of 2.6 (+5.9/−1.1) km Ma^{-1} (ZFT), 2.3 (+2.5/−0.8) (ZHe), 3.7 (+5.4/−2.8) km Ma^{-1} (AFT), as well as 1.7 (+2.1/−1.5) km Ma^{-1} (AHe^1) and 1.5 (+5.6/−0.6) km Ma^{-1} (AHe^2) (Figure 8) (Table 5).

[42] The uncertainties of the slip rate estimates from the fission track data are relatively large but MSWD values of 0.14 and 0.01 are very small while probabilities of fit are close to one (0.873 and 0.937) indicating an overestimation of the analytical errors. The large uncertainties are caused by the relatively large errors of the fission track ages,

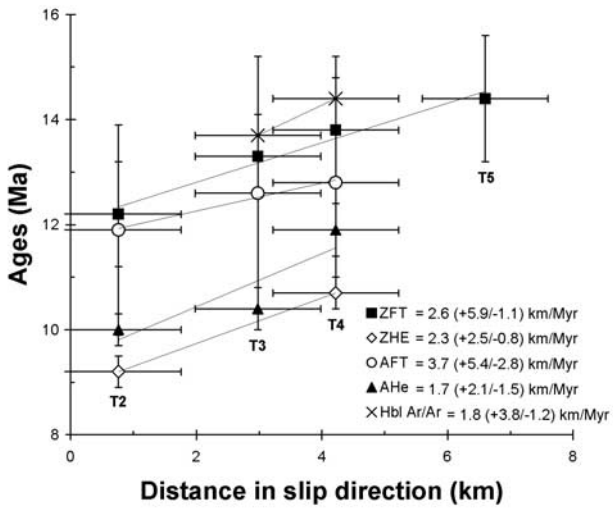

Figure 8. Zircon and apatite fission track (ZFT, AFT), apatite and zircon (U-Th)/He (ZHe, AHe) and $^{40}Ar/^{39}Ar$ hornblende (HAr) ages plotted against distance in slip direction for Livadi detachment. Minimum slip rate for each thermochronometer is shown in lower right.

combined with the small difference in ages and small number of samples. If we consider the fission track data jointly, under the assumption that they record a constant slip rate, the uncertainties fall and the average slip rate becomes 3.2 (+4.0/−1.5) km Ma^{-1}. The AHe data with a MSWD of 3.86 and a low probability of fit (0.003) indicate a significant mismatch, which may reflect additional nonquantified errors in the data. The problem with the AHe data is that the 6% error does not integrate the dispersion of the AHe replicate ages, leading to a high MSWD on the slip rate due to underestimation of the age uncertainties. To solve this problem, we used the standard deviation as the error on the ages. This results in a slip rate of 1.5 (+5.6/−0.6) km Ma^{-1} (AHe^2) with a much higher probability of fit of 0.19 and a much lower MSDW of 1.68. We consider the latter slip rate estimate more reasonable (Figure 8).

[43] The age trend of the $^{40}Ar/^{39}Ar$ hornblende ages depicts the same younging trend as that of the low-temperature thermochronometric ages. If we derived a slip rate from the hornblende data, it would be in the same range as the slip rates derived from the other data sets (Figure 8). Note that a hornblende-derived slip rate of 1.8 (+3.8/−1.2) km Ma^{-1} would most probably be underestimated due to footwall heat advection which has an effect on high-temperature-derived slip rates [*Ketcham*, 1996; *Brichau et al.*, 2006]. However, the problem is that we have not enough hornblende ages to be confident about a consistent northeastward younging trend of ages but we tentatively assume that the hornblende ages show the same general age pattern as the low-temperature data.

[44] The U-Pb zircon, $^{40}Ar/^{39}Ar$ hornblende and the ZFT, ZHe, AFT and AHe ages from the samples collected in the Tinos granites in part overlap within 2σ error and together with the long apatite track length data support very rapid cooling from ~680°C to ~40°C within ~3–4 Ma yielding a crude average cooling rate of ~150–200°C Ma^{-1} (Figure 9). However, the ages from the apatite low-temperature chronometers indicate cooling from ~120°C to ~40°C within <2.5 Ma and yield a minimum cooling rate of ~40°C Ma^{-1} for the Tinos granites. In conjunction with the structural data, this suggests to us that the granites intruded synkinematically into relatively high crustal levels and initially cooled very fast. With time they lost their potential for rapid cooling causing a slow down of the cooling rate.

[45] The path shown for sample T3 is the most well constrained one and thus deserves some more discussion. The U-Pb zircon age is relatively old and if a curve was drawn through the actual age points of the data (not considering any errors) the cooling path (path 1 in Figure 9) would take on an initially convex shape indicating relatively slow cooling just after granite emplacement. This would be somewhat in contradiction to the interpretation of synkinematic emplacement of the granite because an upper crustal granite intruding the footwall of an extensional fault should cool rapidly directly after its emplacement. In a recent paper on the Mykonos monzogranite [*Brichau et al.*, 2007] we argue that granite cooling was controlled by fast slip on the Mykonos detachment, and that peri-plutonic cooling of the Mykonos monzogranite occurred in less than 20–25 ka. To us, path 1 would be more consistent with granite emplacement followed shortly afterward by the onset of extension. Considering 2σ errors, path 2 in Figure 9 is also permissible and we think that this path is more likely because it is in accord with the structural data and the cooling curves inferred for samples T2 and T4. Nonetheless, the errors of

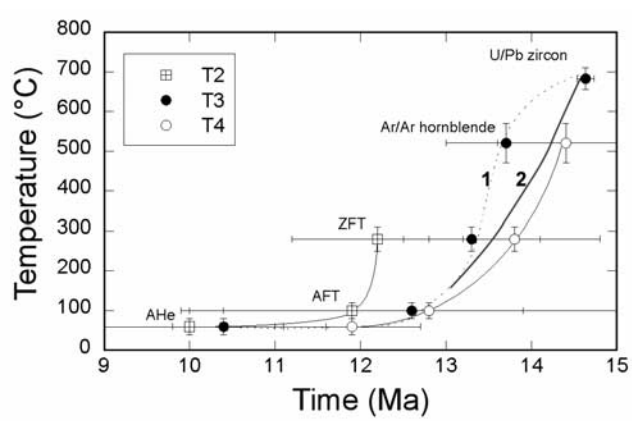

Figure 9. Cooling curves for granite samples from footwall of Livadi detachment. Thermal history is defined by U-Pb zircon (sample T3 only), $^{40}Ar/^{39}Ar$ hornblende (except for sample T2), ZFT, AFT, and AHe ages. For sample T3, two permissible curves (paths 1 and 2) are shown (note that U-Pb zircon and $^{40}Ar/^{39}Ar$ hornblende ages just overlap when 2σ errors are considered); we regard path 2 more likely.

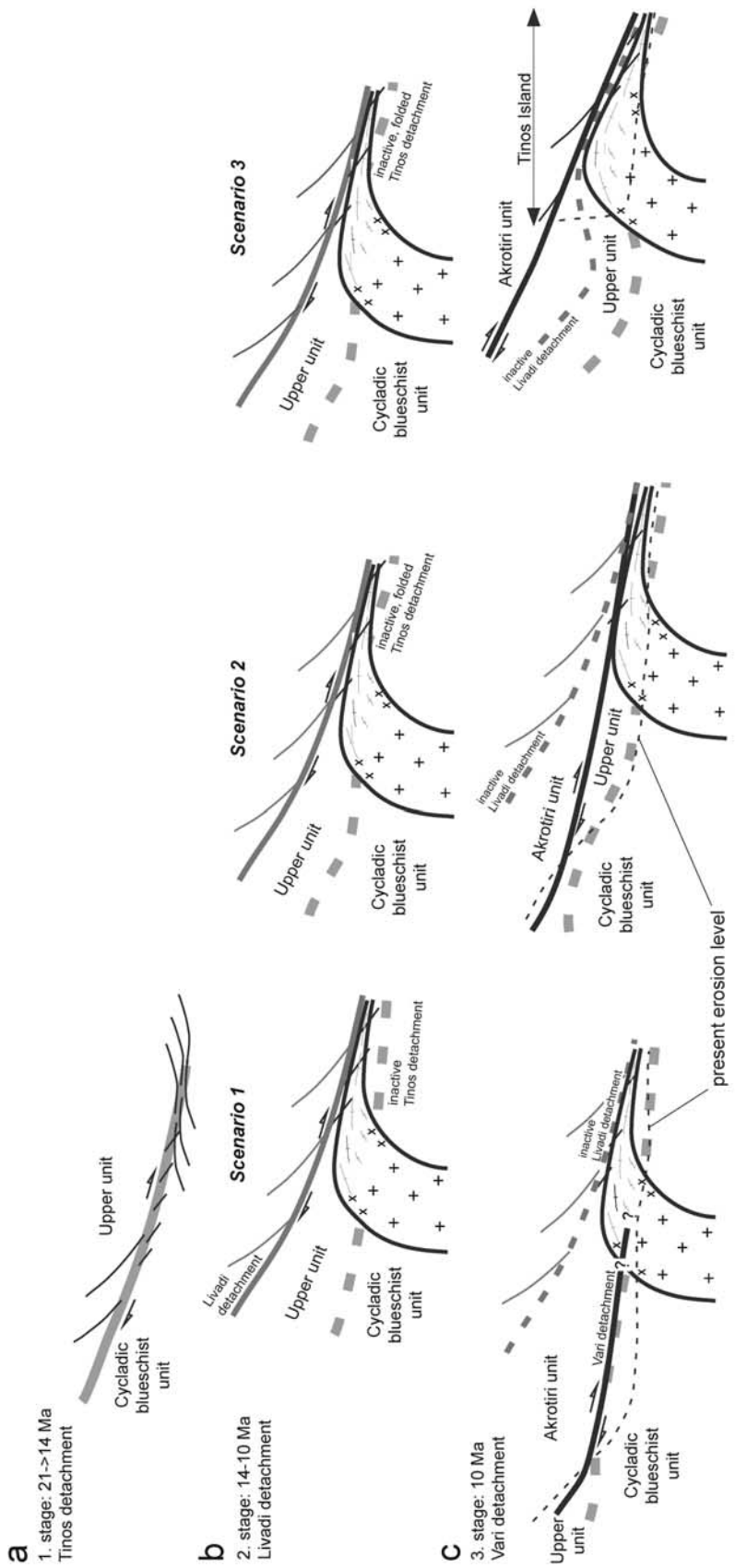

Figure 10. Interpretative cartoons showing envisaged evolution of extensional detachments on Tinos Island. Sketches and timing information on left may imply continuous extension from 21 to 10 Ma; note that geochronologic techniques used do not allow detecting episodic movement on faults. (a) Tinos detachment juxtaposition upper unit above Cycladic blueschist unit. Age data are from *Bröcker and Franz* [1998], and crosscutting Tinos granites constrain this stage to between ~21 and >14 Ma. (b) Low-temperature thermochronology indicating rapid tectonically controlled cooling of Tinos granites between ~14 and 10 Ma due to movement on Livadi detachment. Note that Tinos detachment became inactive and may or may not have been folded at this stage (scenarios 1–3, respectively). (c) Fission track data of *Ring et al.* [2003a] that demand exhumation of ophiolitic mélange of Cycladic blueschist unit at ~10 Ma and imply activity of a third (Vari) detachment. Because of unknown geometry of general structure after earlier stages of faulting, various scenarios are permissible (scenarios 1–3); note that Vari detachment may have partly reactivated earlier detachment planes in all interpretations; note also that in scenarios 1 and 2, Vari detachment cuts into footwall of Livadi detachment; in scenario 3 it cut into hanging wall; scenario 3 does not well explain late cooling of Cycladic blueschist unit at ~10 Ma.

our geochronologic data set do not allow us to rigorously distinguish between path 1 and 2 in Figure 9.

7. Discussion

7.1. How Many Detachments?

[46] The spatial distribution of the low-temperature cooling ages does not seem to be consistent with movement on a single Tinos detachment nor with movement on two detachments (Tinos and Vari detachments). The ZFT ages of 10.2 ± 1.2 Ma and 10.1 ± 0.7 Ma reported by *Ring et al.* [2003a] from southern Tinos do not fit into a tectonically controlled northeastward younging pattern caused by the same detachment that was responsible for rapid tectonically controlled cooling of the Tinos granites in the northeastern part of the island at ~14–10 Ma. Therefore the fission track and (U-Th)/He ages imply that two brittle detachments were active at different stages between ~14 and 10 Ma, which we refer to as the Livadi and Vari detachments (see above). Given that mylonitization and cataclastic deformation at the Tinos detachment occurred between ~21 and >14 Ma, at least three detachment systems must have been active on Tinos Island in the Miocene. The direction and sense of shear during extensional deformation along the various detachments remained the same between ~21 and 10 Ma.

[47] Figure 10 illustrates our interpretation of the timing and geometry of the various extensional detachments on Tinos Island. Greenschist-facies deformation on the Tinos detachment brought the upper unit above the Cycladic blueschist unit (Figure 10a). Stitching of the mylonitic contact by the Tinos granites occurred at ~14.5 Ma. The low-temperature thermochronologic data indicate rapid tectonically controlled cooling of the Tinos granites between ~14 and 10 Ma. Our interpretation is that this cooling and ductile/brittle deformation of the granites is due to movement on Livadi detachment above the granites. Whether or not the Tinos detachment became inactive at this stage, was cataclastically reworked and/or has been folded (scenarios 1–3 in Figures 10b and 10c) cannot be conclusively answered. The fission track data of *Ring et al.* [2003a] demand exhumation of the ophiolitic mélange of the Cycladic blueschist unit in southern Tinos through the brittle-ductile transition at ~10 Ma. Because the granites in northern Tinos already cooled below ~40°C at this stage, the data suggest the operation of a third detachment, the Vari detachment of *Ring et al.* [2003a]. Because of the unknown geometry of the overall structure after the earlier stages of extensional faulting, various scenarios are permissible. All scenarios envisage that upper plate deformation related to the various detachments was distributed over a broad area, with high-angle normal faults rooting in the lower-angle ductile-to-brittle deforming detachment interface. In scenario 1, the Vari detachment cuts downward to the NE causing final cooling of the Cycladic blueschist unit through 280 ± 30°C at ~10 Ma and brittle deformation of the latter in southern Tinos. The Vari detachment juxtaposes the Akrotiri unit above the upper unit. In this interpretation the Vari detachment cuts into the granites, for which there is so far no field evidence. Therefore scenario 2 envisages a folded Tinos detachment that is not being cut by the Vari detachment on Tinos Island. This geometry allows the Vari detachment to emplace the Akrotiri unit above the upper unit without cutting through the Tinos detachment. Accordingly, the Vari detachment can be regarded as part of the Livadi detachment being a younger splay that cut downward into the footwall of the Livadi detachment. Scenario 3 envisages that continued magmatism related to heterogeneous extension resulted in doming, uplift, bending and tilting of the initial detachment horizon [*Miller*, 2003; *Thomson and Ring*, 2006]. In this interpretation, footwall magmatism caused uplift and doming of the Livadi footwall and the cessation of extension by ~12–10 Ma, largely coeval with the emplacement of widespread dikes at ~12–11 Ma [*Avigad et al.*, 1998]. The Vari detachment could then have cut into the hanging wall of the Livadi detachment (Figure 10c, scenario 3). A similar evolution of detachment faulting has been proposed by *Kumerics et al.* [2005] for the Messaria extensional system on Ikaria Island in the eastern Aegean. However, scenario 3 does not explain well the late cooling of the Cycladic blueschist unit at ~10 Ma in southern Tinos.

[48] We consider scenario 2 most likely. Note that in all three interpretations the Vari detachment may have partly reactivated earlier detachment planes implying to some degree episodic movement on the reactivated detachment planes. Resetting of the Rb-Sr biotite ages in the contact aureole of the granites at 10–8 Ma [*Bröcker and Franz*, 2000] is most probably due to deformation related to the Vari detachment [*Ring et al.*, 2003a] and supports scenario 2 by suggesting that the Vari detachment reactivated and/or is a younger footwall splay of the Livadi detachment.

[49] Our low-temperature thermochronologic data indicate heterogeneous and distributed brittle extensional faulting on Tinos Island and together with the fission track data reported by *Ring et al.* [2003a] do not support a continuous and smooth final exhumation of the Cycladic blueschist unit below one single sharp detachment plane. Therefore our data are at variance with the relatively simple progression of extensional deformation from ductile to brittle conditions and localization of deformation into a single (Tinos) detachment as envisaged by *Mehl et al.* [2005]. In the tectonic models advocated in Figure 10 we favor repeated localization of deformation into at least three extensional detachments. We cannot fully rule out that the Tinos, Livadi and Vari detachments belong to one single, very heterogeneous extensional fault system in which localization of deformation repeatedly jumped structurally upward and downward between ~21 and 10 Ma.

7.2. Magmatism, Brittle-Ductile Transition and Slow Slip on the Livadi Detachment

[50] Did extension as the result of subduction zone retreat initiate melting that further enhanced extension?, or did melting induced by accelerated slab retreat result in crustal weakening causing the development of extensional faulting? Our data and the geologic relationships between the

Tinos detachment, the intrusion of the Tinos granites and the Livadi and Vari detachments favor the first option. We discuss the evolution of the detachments on Tinos in relation to the brittle-ductile transition zone, which acts as a weak zone of localized deformation, fluid circulation and pluton emplacement [*Regenauer-Lieb and Yuen*, 2004] and in which some Aegean detachments root [*Ring et al.*, 2003a, 2003b; *Kumerics et al.*, 2005]. We argue that the brittle-ductile transition may in part have played an important role in the successive development of the Livadi and Vari detachments on Tinos Island. We realize that our views are to some extent model driven.

[51] The Tinos detachment formed before the intrusion of the arc-related Tinos granites in a cold fore-arc position at relatively great depths. Our structural data and those of *Avigad and Garfunkel* [1989], *Patriat and Jolivet* [1998], and *Zeffren et al.* [2005] show that there is a greenschist-facies ductile shear zone below and above the Tinos detachment indicating that this detachment does *not* root in the brittle-ductile transition zone but in the ductile crust. Structural relationships indicate that the Tinos detachment sits directly above the Basal unit northwest of Panormos. Because high-pressure metamorphism in the Basal unit occurred at 24–21 Ma and the Tinos detachment was active at ~21 Ma, it must have operated fairly deep in the crust (~30 km as inferred from the barometric estimates given above) and was important for the exhumation of the high-pressure rocks of the Cycladic blueschist unit and especially for those of the Basal unit on Tinos.

[52] The arc-related Tinos granites are synkinematic to the Livadi detachment. Magmatic activity resulted in a transient increase in the geothermal gradient causing the brittle-ductile transition zone to move considerably upward. Thermal weakening caused localization of deformation and the development of a new (Livadi) detachment on Tinos Island probably in the brittle-ductile transition zone and above the older Tinos detachment. *Ring and Collins* [2005] speculated that the intrusion of huge granites in the footwall of the Simav detachment in western Turkey changed the stress geometry and rheology in a way that the detachment became eventually locked. The envisaged bending and locking of the Livadi detachment might have actually been responsible for the initiation of the successive Vari detachment (Figure 10). We favor the idea that the Vari detachment developed in the footwall of the Livadi detachment, again in the brittle-ductile transition zone as previously suggested by *Ring et al.* [2003a] based on the relationship between structures, metamorphism and ZFT ages. Continued magmatic activity documented by the dacitic dikes probably kept the brittle-ductile transition at a relatively high crustal level. Because the footwall of the Livadi detachment was already high up in the brittle crust (with its exhumed fossil brittle-ductile transition zone), localization of the new Vari detachment in the brittle-ductile transition may have caused its development in the footwall of the earlier Livadi detachment.

[53] In contrast to other Aegean detachments, the intrusion of hot magma did apparently not aid fast slip. The slip rate for the Livadi detachment remained fairly constant at ~2.6 (+3.3/−1.0) km Ma^{-1} between the intrusion of the Tinos granites at ~14 Ma and their cooling through ~40°C at ~10 Ma. The data supply a crude displacement of ~10 km between ~14 and 10 Ma. Both slip rate and the offset on the Livadi detachment between ~14 and 10 Ma are distinctly smaller than the slip rate estimate of ~6.5 km Ma^{-1} and >20 km offset for the Vari detachment [*Ring et al.*, 2003a], which postdates any magmatic activity in the region. The locking of the Livadi detachment does not necessarily explain why it slipped relatively slow. A reason for slow slip might be that the Livadi detachment did not reactivate an earlier thrust plane. It is a common observation in the Aegean that rapidly slipping low-angle normal faults reactivated earlier thrust faults and this strongly aided easy and fast slip along shallowly dipping planes [*Lee and Lister*, 1992; *Lister and Forster*, 1996; *Ring et al.*, 2001; *Kumerics et al.*, 2005; *Ring and Collins*, 2005; *Forster and Lister*, 1999; *Thomson and Ring*, 2006]. *Gessner et al.* [2001] showed that the relatively slowly slipping Kuzey detachment in western Turkey did also not reactivate an earlier thrust plane and slip on this detachment was not easy and therefore may have not exceeded 2 km Ma^{-1}.

8. Conclusions

[54] New low-temperature geochronologic data suggest that there are at least three Miocene extensional detachments on Tinos Island. We showed that rapid, tectonically controlled cooling of the Tinos granites was caused by the Livadi detachment which slipped at a relatively slow time-averaged rate of 2.6 (+3.3/−1.0) km Ma^{-1}. At ~10 Ma the younger Vari detachment formed, most probably in the footwall of the Livadi detachment, thereby successively exhuming deeper structural units leading to the final exhumation of the Cycladic blueschist unit through the brittle-ductile transition zone. Our geochronologic data in conjunction with previously published fission track data from Tinos Island show the importance of gaining quantitative thermochronologic data for constraining localization processes of extensional detachments.

[55] **Acknowledgments.** Funded by the Deutsche Forschungsgemeinschaft (grants Ri 538/16, /18, /23 and Graduiertenkolleg 392), and NSF grant EAR-0414817 to Stockli for supporting the zircon (U-Th)/He dating at the University of Kansas. We are grateful to K. A. Farley and L. Hedges for assistance and forbearance during apatite (U-Th)/He dating at California Institute of Technology. The journal reviewers provided useful and constructive comments that helped to revise the paper.

References

Altherr, R., H. Kreuzer, I. Wendt, H. Lenz, G. H. Wagner, J. Keller, W. Harre, and A. Höhndorf (1982), A late Oligocene/early Miocene high temperature belt in the Attic-Cycladic crystalline complex (SE Pelagonian, Greece), *Geol. Jahrb., Reihe E*, *23*, 97–164.

Avigad, D., and T. Garfunkel (1989), Low-angle faults above and below a blueschist belt–Tinos Island, Cyclades, Greece, *Terra Nova*, *1*, 182–187.

Avigad, D., G. Baer, and A. Heimann (1998), Block rotations and continental extension in the central Aegean Sea: palaeomagnetic and structural evidence from Tinos and Mykonos (Cyclades, Greece), *Earth Planet. Sci. Lett.*, *157*, 23–40.

Ballard, J. R., J. M. Palin, I. S. Williams, and I. H. Campbell (2001), Two ages of porphyry intrusion resolved for the super-giant Chuquicamata copper deposit in northern Chile by ELA-ICP-MS and SHRIMP, *Geology*, *29*, 383–386.

Barbarand, J., A. Carter, I. Wood, and T. Hurford (2003), Compositional and structural control of fission-track annealing in apatite, *Chem. Geol.*, *198*, 107–137.

Black, L. P., S. L. Kamo, C. M. Allen, J. N. Aleinikoff, D. W. Davis, R. J. Korsch, and C. Foudoulis (2003), TEMORA 1: A new zircon standard for Phanerozoic U-Pb geochronology, *Chem. Geol.*, *200*, 155–170.

Boven, A., P. Pasteels, S. P. Kelley, L. Punzalan, B. Bingen, and D. Demaiffe (2001), $^{40}Ar/^{39}Ar$ study of plagioclases from the Rogaland anorthosite complex (SW Norway); an attempt to understand argon ages in plutonic plagioclase, *Chem. Geol.*, *176*, 105–135.

Brichau, S., U. Ring, R. A. Ketcham, A. Carter, D. Stockli, and M. Brunel (2006), Constraining the long-term evolution of the slip rate for a major extensional fault system in the central Aegean, Greece, using thermochronology, *Earth Planet. Sci. Lett.*, *241*, 293–306.

Brichau, S., U. Ring, A. Carter, R. Bolhar, P. Monie, S. N. Thomson, D. Stockli, and M. Brunel (2007), Timing, slip rate, displacement and cooling history of the Mykonos detachment footwall, Cyclades, Greece, and implications for the opening of the Aegean Sea, *J. Geol. Soc. London*, in press.

Bröcker, M., and L. Franz (1998), Rb-Sr isotope studies on Tinos Island (Cyclades, Greece): additional time constraints for metamorphism, extent of infiltration-controlled overprinting and deformational activity, *Geol. Mag.*, *135*, 369–382.

Bröcker, M., and L. Franz (2000), The contact aureole on Tinos (Cyclades, Greece): Tourmaline-biotite geothermometry and Rb-Sr geochronology, *Mineral. Petrol.*, *70*, 257–283.

Clauer, N., J. R. O'Neil, and C. Bonnot-Courtois (1982), The effect of natural weathering on the chemical and isotopic compositions of biotites, *Geochim. Cosmochim. Acta*, *46*, 1755–1762.

Compston, W., I. S. Williams, and C. Meyer (1984), U-Pb geochronology of zircons from lunar breccia 73217 using a sensitive high mass-resolution ion microprobe, *Proc. Lunar Planet. Sci. Conf. 14th*, Part 2, *J. Geophys. Res.*, *89*, suppl., B525–B524.

Coulson, I. M., M. E. Villeneuve, G. M. Dipple, R. A. Duncan, J. K. Russell, and J. K. Mortensen (2002), Time-scales of assembly and thermal history of a composite felsic pluton: constraints from the Emerald Lake area, northern Canadian Cordillera, Yukon, *J. Volcanol. Geotherm. Res.*, *114*, 331–356.

Dahl, P. S. (1996), The effects of composition on retentivity of argon and oxygen in hornblende and related amphiboles: A field-tested empirical model, *Geochim. Cosmochim. Acta*, *60*, 3687–3700.

Donelick, R. A., and D. S. Miller (1991), Enhanced TINT fission track densities in low spontaneous track density apatites using ^{252}Cf-derived fission fragment tracks: a model and experimental observation, *Nucl. Tracks Radiat. Meas.*, *18*, 301–307.

Dürr, S., R. Altherr, J. Keller, M. Okrusch, and E. Seidel (1978), The median Aegean crystalline belt: Stratigraphy, structure, metamorphism, magmatism, in *Alps, Appeninnes, Hellenides*, edited by H. Closs, D. Roeder, and K. Schmidt, *Sci. Rep. 38*, pp. 455–477, Inter-Union Comm. on Geodyn., Stuttgart, Germany.

Esser, R. P., W. C. McIntosh, M. T. Heizler, and P. R. Kyle (1997), Excess argon in melt inclusions in zero-age anorthoclase feldspar from Mt. Erebus, Antarctica, as revealed by the $^{40}Ar/^{39}Ar$ method, *Geochim. Cosmochim. Acta*, *61*, 3789–3801.

Farley, K. A., R. A. Wolf, and L. T. Silver (1996), The effects of long alpha-stopping distances on (U-Th)/He ages, *Geochim. Cosmochim. Acta*, *60*, 4223–4229.

Faure, M., M. Bonneau, and J. Pons (1991), Ductile deformation and syntectonic granite emplacement during the late Miocene extension of the Aegea (Greece), *Bull. Soc. Geol. Fr.*, *162*, 3–11.

Forster, M. A., and G. S. Lister (1999), Detachment faults in the Aegean core complex of Ios, Cyclades, Greece, in *Exhumation Processes: Normal Faulting, Ductile Flow and Erosion*, edited by U. Ring et al., *Geol. Soc. Spec. Publ.*, *154*, 305–323.

Foster, D. A., and B. E. John (1999), Quantifying tectonic exhumation in an extensional orogen with thermochronology: examples from the southern Basin and Range province, in *Exhumation Processes: Normal Faulting, Ductile Flow and Erosion*, edited by U. Ring et al., *Geol. Soc. Spec. Publ.*, *154*, 343–364.

Fytikas, M., F. Innocenti, P. Manetti, R. Mazzuoli, A. Peccerillo, and L. Villari (1984), Tertiary to Quaternary evolution of volcanism in the Aegean region, in *The Geological Evolution of the Eastern Mediterranean*, edited by A. H. F. Robertson and J. E. Dixon, *Geol. Soc. Spec. Publ.*, *17*, 687–699.

Galbraith, R. F., and G. M. Laslett (1993), Statistical models for mixed fission track age, *Nucl. Tracks Radiat. Meas.*, *21*, 459–470.

Gessner, K., U. Ring, C. Johnson, R. Hetzel, C. W. Passchier, and T. Güngör (2001), An active bivergent rolling-hinge detachment system: The central Menderes metamorphic core complex in western Turkey, *Geology*, *29*, 611–614.

Godfriaux, I. (1968), Etude géologique de la région de l'Olympe (Gréce), *Ann. Geol. Pays Hell.*, *19*, 1–271.

Green, P. F., I. R. Duddy, G. M. Laslett, K. A. Hegarty, A. J. W. Gleadow, and J. F. Lovering (1989), Thermal annealing of fission tracks in apatite, 4, Quantitative modelling techniques and extension to geological timescale, *J. Pet. Geol.*, *12*, 111–114.

Hejl, E., H. Riedl, and H. Weingartner (2002), Post-plutonic unroofing and morphogenesis of the Attic-Cycladic complex (Aegea, Greece), *Tectonophysics*, *349*, 37–56.

Hourigan, J. K., P. W. Reiners, and M. T. Brandon (2005), U-Th zonation-dependent alpha-ejection in (U-Th)/He chronometry, *Geochim. Cosmochim. Acta*, *69*, 3349–3365.

House, M. A., K. A. Farley, and D. Stockli (2000), Helium chronometry of apatite and titanite using Nd-YAG laser heating, *Earth Planet. Sci. Lett.*, *183*, 365–368.

Hurford, A. J. (1990), Standardisation of fission-track dating calibration: Recommendation by the Fission Track Working Group of the I.U.G.S. Subcommission on Geochronology, *Chem. Geol.*, *80*, 171–178.

Hurford, A. J., and P. F. Green (1983), The zeta age calibration of fission-track dating, *Chem. Geol.*, *1*, 285–317.

John, B. E., and K. A. Howard (1995), Rapid extension recorded by cooling-age patterns and brittle deformation, Naxos, Greece, *J. Geophys. Res.*, *100*, 9969–9979.

Keay, S. (1998), The geological evolution of the Cyclades, Greece: Constraints from SHRIMP U-Pb geochronology, Ph.D. thesis, 341 pp., Aust. Natl. Univ., Canberra.

Kelley, S. P. (2002), K-Ar and Ar-Ar dating, in *Noble Gases in Geochemistry and Cosmochemistry*, *Rev. Mineral. Geochem.*, vol. 47, edited by D. P. Porcielli, C. J. Ballentina, and R. Wierler, pp. 431–485, Mineral. Soc. of Am., Washington, D. C.

Ketcham, R. A. (1996), Thermal models of core-complex evolution in Arizona and New Guinea: Implications for ancient cooling paths and present-day heat flow, *Tectonics*, *15*, 933–951.

Ketcham, R. A., R. A. Donelick, and W. D. Carlson (1999), Variability of apatite fission-track annealing kinetics; III, Extrapolation to geological time scales, *Am. Mineral.*, *84*, 1235–1255.

Kumerics, C., U. Ring, S. Brichau, J. Glodny, and J.-P. Monie (2005), The extensional Ikaria shear zone and associated brittle detachments faults, Aegean Sea, Greece, *J. Geol. Soc. London*, *162*, 701–721.

Lee, J., and G. S. Lister (1992), Late Miocene ductile extension and detachment faulting, Mykonos, Greece, *Geology*, *20*, 121–124.

Lister, G. S., and M. Forster (1996), Inside the Aegean metamorphic core complexes, *Tech. Publ. 45*, 110 pp., Aust. Crustal Res. Centre, Clayton, Victoria.

Lister, G. S., G. Banga, and A. Feenstra (1984), Metamorphic core complexes of Cordilleran type in the Cyclades, Aegean Sea, Greece, *Geology*, *12*, 21–25.

Ludwig, K. R. (2003), Isoplot, A geochronological toolkit for Microsoft Excel, version 3.0, *Spec. Publ. 4*, 70 pp. Berkeley Geochronol. Cent., Berkeley, Calif.

Maluski, H., M. Bonneau, and J. R. Kienast (1987), Dating the metamorphic events in the Cycladic area: $^{39}Ar/^{40}Ar$ data from metamorphic rocks of the island of Syros (Greece), *Bull. Soc. Geol. Fr.*, *5*, 833–842.

Mehl, C., L. Jolivet, and O. Lacombe (2005), From ductile to brittle: Evolution and localization of deformation below a crustal detachment (Tinos, Cyclades, Greece), *Tectonics*, *24*, TC4017, doi:10.1029/2004TC001767.

Melidonis, N. G. (1980), The geological structure and mineral deposits of Tinos island (Cyclades, Greece), *Geol. Greece*, *13*, 1–80.

Miller, M. (2003), Basement involved thrust faulting in a thin-skinned fold and thrust belt, Death Valley, California, USA, *Geology*, *31*, 31–34.

Patriat, M., and L. Jolivet (1998), Post-orogenic extension and shallow-dipping shear zones, study of a brecciated decollement horizon in Tinos (Cyclades, Greece), *C. R. Acad. Sci.*, *326*, 355–362.

Patzak, M., M. Okrusch, and H. Kreuzer (1994), The Akrotiri unit on the island of Tinos, Cyclades, Greece: witness to a lost terrane of Late Cretaceous age, *Neues Jahrb. Geol. Paleontol. Abh.*, *194*, 211–252.

Pearce, N. J. G., W. T. Perkins, J. A. Westgate, M. P. Gorton, S. E. Jackson, C. R. Neal, and S. P. Chenery (1997), A compilation of new and published major and trace element data for NIST SRM 610 and NIST SRM 612 glass reference materials, *Geostand. Newsl.*, *21*, 115–144.

Rahn, M. K., M. T. Brandon, G. E. Batt, and J. I. Garver (2004), A zero-damage model for fission-track annealing in zircon, *Am. Mineral.*, *89*, 473–484.

Regenauer-Lieb, K., and D. A. Yuen (2004), Positive feedback of interacting ductile faults from coupling of equation of state, rheology and thermal-mechanics, *Phys. Earth Planet Inter.*, *142*, 113–135.

Reiners, P. W. (2005), Zircon (U-Th)/He Thermochronometry, in *Thermochronology Rev. Mineral. Geochem.*, vol. 58, edited by P. W. Reiners and T. A. Ehlers, pp. 151–176, Mineral. Soc. of Am., Washington, D. C.

Ring, U., and A. S. Collins (2005), SHRIMP dating of the syn-tectonic Egrigöz granite: Precise timing of core-complex formation in the Anatolide belt of western Turkey, *J. Geol. Soc. London*, *162*, 289–298.

Ring, U., and P. W. Layer (2003), High-pressure metamorphism in the Aegean, eastern Mediterranean: Underplating and exhumation from the Late Cretaceous until the Miocene to Recent above the retreating Hellenic subduction zone, *Tectonics*, *22*(3), 1022, doi:10.1029/2001TC001350.

Ring, U., and T. Reischmann (2002), The weak and superfast Cretan detachment, Greece: Exhumation at subduction rates in extrusion wedges, *J. Geol. Soc. London*, *159*, 225–228.

Ring, U., S. Laws, and M. Bernet (1999), Structural analysis of a complex nappe sequence and late-orogenic basins from the Aegean Island of Samos, Greece, *J. Struct. Geol.*, *21*, 1575–1601.

Ring, U., P. W. Layer, and T. Reischmann (2001), Miocene high-pressure metamorphism in the Cyclades

and Crete, Aegean Sea, Greece: Evidence for large-magnitude displacement on the Cretan detachment, *Geology*, *29*, 395–398.

Ring, U., S. N. Thomson, and M. Bröcker (2003a), Fast extension but little exhumation: the Vari detachment in the Cyclades, Greece, *Geol. Mag.*, *140*, 245–252.

Ring, U., C. Johnson, R. Hetzel, and K. Gessner (2003b), Tectonic denudation of a Late Cretaceous–Tertiary collisional belt: regionally symmetric cooling patterns and their relation to extensional faults in the Anatolide belt of western Turkey, *Geol. Mag.*, *140*, 421–441.

Ring, U., T. Will, J. Glodny, and S. N. Thomson (2007), An Oligocene extrusion wedge of blueschist-facies nappes on Evia Island, Aegean Sea, Greece: Implications for the early exhumation of high-pressure rocks, *J. Geol. Soc. London*, *164*, 637–657, doi:10.1144/0016-76492006-041.

Robertson, A. H. F., P. Clift, P. J. Degnan, and G. Jones (1991), Palaeogeographic and palaeotectonic evolution of the eastern Mediterranean Neotethys, *Palaeogeogr. Palaeoclimatol. Palaeoecol.*, *87*, 243–289.

Samson, S. D., and E. C. Alexander (1987), Calibration of the interlaboratory ^{40}Ar-^{39}Ar dating standard, MMhb-1, *Chem. Geol.*, *66*, 34–37.

Schmädicke, E., and T. M. Will (2003), Pressure-temperature evolution of blueschist facies rock from Sifnos, Greece, and implications for the exhumation of high-pressure rocks in the central Aegean, *J. Metamorph. Geol.*, *21*, 799–811.

Shaked, Y., D. Avigad, and Z. Garfunkel (2000), Alpine high-pressure metamorphism at the Almyropotamos window (southern Evia, Greece), *Geol. Mag.*, *137*, 367–380.

Stern, R. A., and Y. Amelin (2003), Assessment of errors in SIMS zircon U-Pb geochronology using a natural zircon standard and NIST SRM 610 glass, *Chem. Geol.*, *197*, 111–142.

Stöckhert, B., M. R. Brix, R. Kleinschrodt, A. J. Hurford, and R. Wirth (1999), Thermochronometry and microstructures of quartz; a comparison with experimental flow laws and predictions on the temperature of the brittle-plastic transition, *J. Struct. Geol.*, *21*, 351–369.

Stockli, D. F. (2005), Application of low-temperature thermochronometry to extensional tectonic settings, in *Low-Temperature Thermochronology; Techniques, Interpretations, and Applications*, *Rev. Mineral. Geochem.*, vol. 58, edited by P. W. Reiners and T. A. Ehlers, pp. 411–448, Mineral. Soc. of Am., Washington, D. C.

Stockli, D. F., K. A. Farley, and T. A. Dumitru (2000), Calibration of the (U-Th)/He thermochronometer on an exhumed normal fault block in the White Mountains, eastern California and western Nevada, *Geology*, *28*, 983–986.

Tagami, T., R. F. Galbraith, R. Yamada, and G. M. Laslett (1998), Revised annealing kinetics of fission tracks in zircon and geological implications, in *Advances in Fission-Track Geochronology*, edited by P. Van Den Haute and F. De Corte, pp. 99–112, Kluwer Acad., Dordrecht, Netherlands.

Thomson, S. N., and U. Ring (2006), Thermochronologic evaluation of postcollision extension in the Anatolide orogen, western Turkey, *Tectonics*, *25*, TC3005, doi:10.1029/2005TC001833.

Tomaschek, F., A. Kennedy, I. M. Villa, and C. Ballhaus (2003), Zircons from Syros, Cyclades, Greece: Recrystallization and mobilisation during high pressure metamorphism, *J. Petrol.*, *44*, 1977–2002.

Villa, I. M. (1998), Isotopic closure, *Terra Nova*, *10*, 42–47.

Watson, E. B., D. A. Wark, and J. B. Thomas (2006), Crystallisation thermometers for zircon and rutile, *Contrib. Mineral. Petrol.*, *151*, 413–433.

Weidmann, M., N. Solounias, R. E. Drake, and G. H. Curtis (1984), Neogene stratigraphy of the eastern basin, Samos island, Greece, *Geobios*, *17*, 477–490.

Wijbrans, J. R., M. Schliestedt, and D. York (1990), Single grain argon laser probe dating of phengites from the blueschist to greenschist transition on Sifnos (Cyclades, Greece), *Contrib. Mineral. Petrol.*, *104*, 582–593.

York, D. (1969), Least squares fitting of a straight line with correlated errors, *Earth Planet. Sci. Lett.*, *5*, 320–324.

Zeffren, S., D. Avigad, A. Heimann, and Z. Gvirtzman (2005), Age resetting of hanging wall rocks above a low-angle detachment fault: Tinos Island (Aegean Sea), *Tectonophysics*, *400*, 1–25, doi:10.1016/j.tecto.2005.01.003.

R. Bolhar and U. Ring, Department of Geological Sciences, University of Canterbury, Christchurch 8140, New Zealand.

S. Brichau and A. Carter, School of Earth Sciences, University and Birkbeck College, Malet Street, London WC1E 7HX, UK. (s.brichau@bbk.ac.uk)

M. Brunel and P. Monié, Laboratoire Dynamique de la lithosphère, UMR-CNRS 5573, Université Montpellier II, 34095 Montpellier Cedex 05, France.

D. Stockli, Department of Geology, University of Kansas, Lawrence, KS 66045, USA.